UNIVERSITÀ DEGLI STUDI DI PALERMO

DIPARTIMENTO DI ENERGIA, INGEGNERIA DELL'INFORMAZIONE
E MODELLI MATEMATICI

Corso di Dottorato in Ingegneria Elettronica e delle Telecomunicazioni

Settore scientifico disciplinare: ING-INF/01

TESI DI DOTTORATO

"FREE SPACE OPTICS LINKS AFFECTED BY OPTICAL TURBULENCE: CHANNEL MODELING, MEASUREMENTS AND CODING TECHNIQUES FOR ERROR MITIGATION"

Candidato

Ing. Andrea Andò

Coordinatore del Dottorato

Prof. Giovanni Garbo

Tutor

Prof. Alessandro Busacca

XXIV Ciclo – Triennio 2011 - 2013

DOTTORATO

Contents

Summary

FSO is an optical wireless line-of-sight communication system able to offer good broadband performance, electromagnetic interference immunity, high security, license-free operation, low power consumption, ease of relocation, and straightforward installation. It represents a modern technology, significantly functional when it is impossible, expensive or complex to use physical connections or radio links. Unfortunately, since the transmission medium in a terrestrial FSO link is the air, these communications are strongly dependent on various atmospheric phenomena (e.g., rain, snow, optical turbulence and, especially, fog) that can cause losses and fading. Therefore, in worst-case conditions, it could be necessary to increase the optical transmission power, although, at the same time, it is needed to comply to safety regulations. The effects of the already mentioned impairments are: scattering (i.e., Rayleigh and Mie) losses, absorption and scintillation. The first two can be described by proper attenuation coefficients and increase if the atmospheric conditions get worst. As regards scintillation, it is a random phenomenon, appreciable even under clear sky. Because of scintillation, in FSO links, the irradiance fluctuates and could drop below a threshold under which the receiver is not able to detect the useful signal. In this case, communications suffer from erasure errors, which cause link outages. This phenomenon becomes relevant at high distance, but it can also be observed in 500m-long FSO links. Moreover, the optical turbulence intensity can change of an order of magnitude during the day: it reaches its maximum around midday (when the temperature is the highest) and, conversely, it is lower during the night.

In order to reduce or eliminate these impairments, different methods (both hardware and software) were studied and reported in literature. Hardware solutions focus on aperture averaging effects to reduce irradiance fluctuations, in particular by using a bigger detector or multi-detector systems. On the other hand, software techniques mostly focus on transmission codes. Rateless codes are an innovative solution, suitable for channels affected by erasure or burst errors. They add a redundant coding (also settable on the fly) to the source data, allowing the receiver to successfully recover the whole payload that, otherwise, would be corrupted or partially lost. To test rateless codes, recovery capabilities in FSO channels, detailed information about the occurring signal fading are needed: in particular, its depth, temporal duration and statistics. For this reason, I have implemented a time-correlated channel model

able to generate an irradiance time-series at the receiver side, at wide range of turbulence conditions (from weak to strong).

The time-series represents a prediction of temporal irradiance fluctuations caused by scintillation. In this way, I was able to test the recovery capabilities of several types of rateless codes. I have performed measurement campaigns in order to characterize Free Space Optics links affected by the optical turbulence. In particular, I have used three different setups placed in the Laboratory of Optics of the University of Palermo and in the Optical Communication Laboratory of the Northumbria University. Thanks to an in-depth post-processing of the collected data, I was able to extract useful information about the FSO link quality and the turbulence strength, thus proving the effectiveness of the Gamma-Gamma model under several turbulence conditions.

In Chapter 1, I will introduce the theory of optical wireless communications and, in particular, of Free Space Optics communications. In detail, I will describe the advantages and the impairments that characterize this kind of communication and discuss about its applications.

In Chapter 2, the adopted channel models are presented. In particular, these models are able to predict irradiance fluctuations at the detector in Free Space Optics links and were designed for terrestrial and space-to-ground communications at different link specifications, turbulence conditions and temporal covariance. Firstly, a brief description of the employed irradiance distribution and of the irradiance covariance functions is presented. The details of the above mentioned channel model implementation and the performance are then described. Finally, in order to detail the channel model features, several examples of irradiance fluctuation predictions are depicted.

In Chapter 3, the details of a measurement campaign, focused on the analysis of optical turbulence effects in a FSO link, will be treated. Three different measurement setups composed of different typologies of laser sources, detectors and turbulent channels will be described. Data post-processing will be discussed. Moreover, a performance evaluation of the terrestrial channel model described in Chapter 2 will be discussed.

In Chapter 4, rateless codes will be presented. These codes introduce a redundancy by means of repair symbols, associated to the source data, and, in case of losses, they are able to recover the source data without any need for retransmission. They can also manage large

amounts of data and offer very interesting features for erasure channels and multicast/broadcast applications. Three different classes of rateless codes will be described and, in particular: Luby Transform, Raptor and RaptorQ codes.

Moreover, the performance of the rateless codes in Free Space Optics links will be investigated. The implemented simulators are based on the channel models presented in Chapter 2 and focus on the study of rateless codes recovery capabilities when erasure errors due to fadings occur. The results on the performance of three rateless codes typologies, in two different FSO links, will be illustrated.

All the research work was supported by the European Space Agency (grant no. 5401001020). Experimental activities were performed in collaboration with the Optical Communications Research Group of the Northumbria University and within the COST IC1101 European Action.

Chapter 1

"Free Space Optics: theory and applications"

1.1 Introduction

Fiber optics technology is adopted to ensure error-free and high data-rate linked communications, but it is not the most cost effective way to offer high-quality video and audio streaming services to end users. Another important technique that offers a new high-performance methodology and permits to connect cities is the Free Space Optics (FSO) technology. It is cost-effective and easy to deploy, also offering large bandwidth and, electromagnetic immunity. Moreover, FSO has wide practical applications and shows several advantages if compared to radio links, especially in terms of high transmission rates and security. FSO links are employed in terrestrial and satellite communications. FSO terrestrial links are able to cover several kilometers, over horizontal paths and, for this reason, this technology is suitable in the case of rural zones, rivers, highways, etc. [1]. FSO space applications consist in inter/intra-satellite communications and satellite to earth links [2]. Another communication technique is underwater FSO. It is an ongoing technology that already offers some advantages as it does not necessarily need Line of Sight, in fact, using the reflection of the light at the water/air interface, it can cover the same link with different paths [3].

In Free Space Optics links, in order to transmit data through the free space, the optical carrier wavelengths (typically around 850,1060nm and 1550 nm [4]) are intensity-modulated. As mentioned, an important advantage of FSO links is that any interference with Radio transmission apparatuses is absent. However, the transmitted optical signals can be strongly affected by unfavorable atmospheric conditions, such as rain, fog, clouds, snow, smog, aerosol scattering and scintillations. Moreover, FSO links require "line of sight" between the receiver and the transmitter, and any misalignment due to twisting, swaying and bending of structures

can create serious difficulties for remote transmissions [5, 6].

A typical FSO communication system is composed by three main functional elements: the transmitter, the atmospheric channel and the receiver, as illustrated in Figure 1.1.

The transmitter modulates the source data onto the optical carrier which is then transmitted to the receiver through the atmosphere. The modulation is performed by using either a direct modulation (the driving current modulates directly the optical source) or an external modulation. Moreover, the transmitter telescope collects, collimates and directs the optical signal towards the receiver telescope at the other end of the link.

At the receiver, the optical signal is collected by a system of lenses and detected by a photodetector. Generally, this happens in the presence of noise interference, signal distortion, and background radiation. In detail the receiver is usually composed by: a telescope that collects and focuses the incoming optical radiation onto the photodetector; an optical band pass filter which reduces the environmental noise; a photodetector, usually a PIN or an avalanche photodiode, that converts the optical signal into an electrical signal. The above-mentioned scheme can be defined as a Single-Input Single-Output (SISO) system.

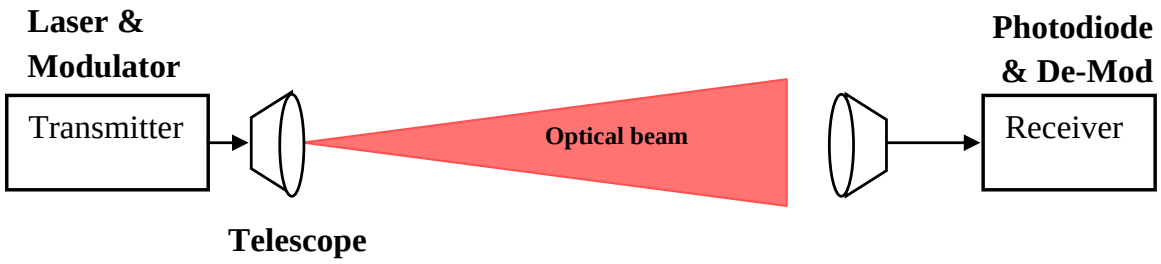

Figure 1.1 – General scheme of a Free Space Optics link.

In order to improve the performance, modern FSO apparatuses can employ more optical source and detectors. FSO links that use this scheme can be defined as a Multiple-Input Multiple-Output (MIMO) systems. These solutions usually present better performance, and on the other hand, are more expensive and complex than the SISO systems [7,8].

1.2 Free Space Optics applications

As already mentioned, FSO links are employed for different communications typologies. In the case of terrestrial communications, the most used scenarios are: LAN network extender, last mile network and Radio on FSO (RoFSO). As regards the first scenario, we suppose that we need to connect the LAN network of two close buildings. In most cases, a FSO link presents the best trade off to solve this problems, as it offers good performance and requires only small economic resources (in this scenario, only two FSO apparatuses are needed). In fact, a physical connection can offers the best performance but it is too expensive, and a radio link is cheaper, but the rate performance should present limits.

FSO technology can be very useful also for the *last mile networks*. The latter represents the portions of a carrier network that connect subscribers directly to the provider equipment [9]. The most common technology used for the last-mile access is the DSL (Digital Subscriber Line) able to provide benefits on the infrastructure with respect to the deployment costs. However, this access method represents a bottleneck between the high-speed residential and business networks and the core backbone network. Passive Optical Networks (PON) are an excellent solution to improve the bandwidth performance of the copper Access Network; moreover, they permit a gradual replacement of the old networks [10]. Unfortunately, the costs of these optical networks are expensive limiting the number of installations in the cities. FSO links are primarily economic, in fact their installation do not require costs as high as those needed to trench the streets and to lay fibers and do not present the recurrent costs associated with leasing fiber lines. Furthermore, FSO terminals can be deployed in places where it is difficult or not possible to lay the fiber, such as town centres, rivers, rail tracks. On the other hand, the FSO technology has the disadvantage to be susceptible to the atmospheric effects (see section 1.3), which can reduce the link availability and may introduce burst errors [11].

Another interesting application of FSO technology is the Radio on Free Space Optics (RoFSO). This technology, that originates from the Radio on Fiber (RoF), permits to transmit heterogeneous RF signals such as: cellular networks, WiFi, WiMax and DTV. It is also possible to simultaneously transmit multiple RF signals (including heterogeneous wireless services) using the Wavelength-Division Multiplexing (WDM) technology. RoFSO can allow the convergence of fiber and free-space optical communication networks, thus extending broadband connectivity to underserved areas [12].

1.3 Atmospheric effects

In most cases, Free-space optics (FSO) uses the atmosphere as the propagation medium. The latter is perturbed by different atmospheric phenomena (e.g., rain, fog, clouds, dust, smoke, smog, etc.) that can affect the transmission of a laser beam through the atmosphere. The most important challenges of the FSO communications, even in clear sky conditions, are: absorption, scattering, and scintillation. These impairments are wavelength dependent and cause -along the FSO links- optical signal losses, irradiance fluctuations, beam broadening, loss of spatial coherence of the optical wave [7].

In detail, absorption causes losses and occurs when a photon is absorbed by an atmospheric gaseous molecule that converts the photon into kinetic energy [6]. Furthermore, the atmospheric absorption strongly depends on the wavelength [5,6]. In the spectral windows used for FSO, the most common absorbing particles are water, carbon dioxide, and ozone. Figure 1.2 shows the space-ground transmittance (also called atmospheric transmission [6]) in the visible and near-infrared (IR) regions [13]. The diagram highlights that only some spectral windows are suitable for the FSO communications. In particular, the windows that present low losses and, for which laser sources are available, are in the spectral range close to wavelengths of 850 nm, 1060 nm and 1550 nm [4].

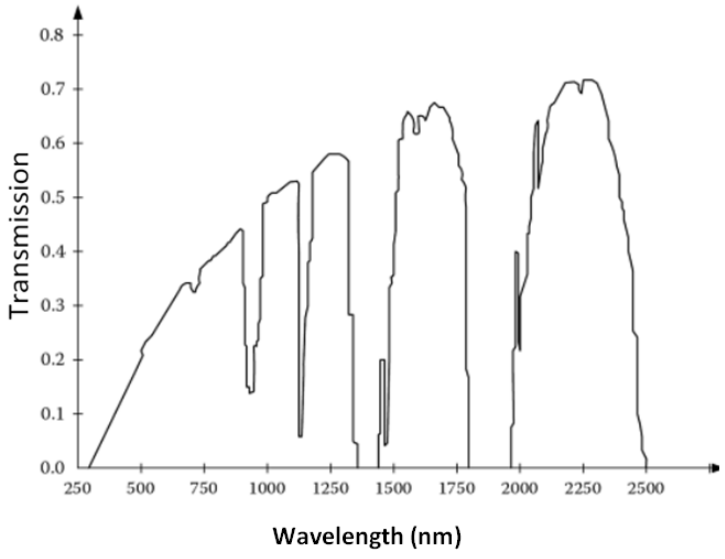

Figure 1.2 – Atmospheric transmission from space to ground at mid-latitude, during the summer time, in visible and near-IR region.

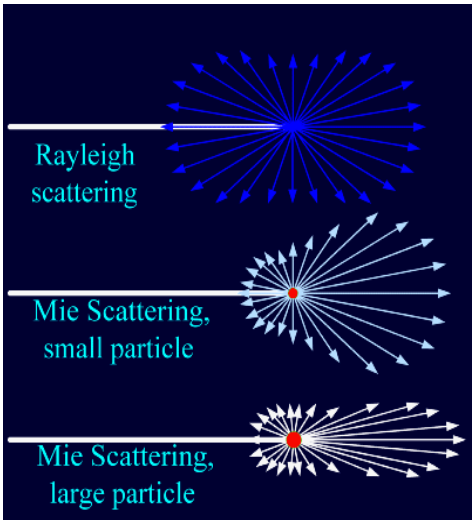

Figure 1.3 – Comparison between Rayleigh and Mie Scattering.

The scattering hydrometeors (rain, fog, snow or clouds) are the main causes of scattering in FSO links [14,15,16]. They introduce high losses, mostly the fog, and limit the FSO link availability. Mie and Rayleigh are the most relevant scattering effects. The first is valid for each scattering center, but it is usually employed when the particle size in the atmosphere is comparable or greater than the wavelength of the optical beam. Pollution, dust, water vapor and smoke are the main responsible for scattering. As a consequence, Mie scattering occurs in the lower layer of the troposphere where such particles are present in higher concentrations [17]. Rayleigh is an approximation of Mie scattering, in the case of single point scattering centers. Therefore, it occurs when the atmospheric molecules show a size much smaller than the wavelength of the incident light. Moreover, the intensity of the scattered light is proportional to λ^{-4} and, so, Rayleigh scattering effects reduce with increasing wavelength.

In addition, Mie and Rayleigh are elastic light scattering in which the frequency of the scattered light is equal to that of the incident beam [18]. However, the distribution of the scattered light is different. As shown in the Figure 1.3, the intensity of the scattered light is largely uniform in the case of Rayleigh scattering, while it is greatest in the direction of the incident light for the Mie scattering case.

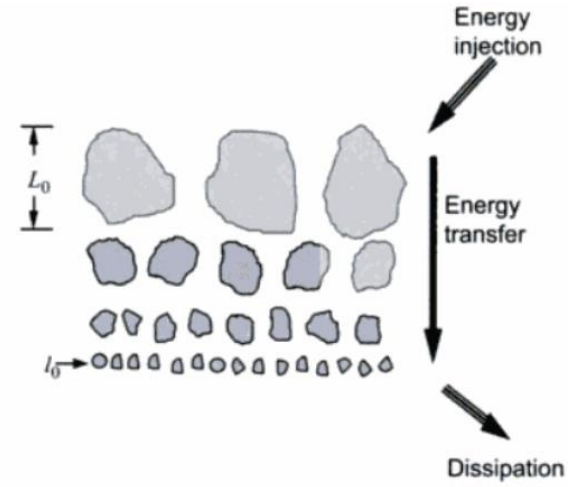

Figure 1.4 – Kolmogorov cascade theory of turbulence, where L_0 denotes the outer scale and l_0 the inner scale [6].

1.4 Optical turbulence

The temperature variations, along the optical path, afflicts the FSO communications. These variations originate refractive index fluctuations (i.e., optical turbulence) that cause distortions to the laser beam wave. This happens when the atmosphere is in a turbulent state. In these conditions, the turbulent air motion is composed by eddies of different scales also known as inner scale l_0 and outer scale L_0. In particular, the eddies size changes from a small to a large scale. Close to the ground, outer scale increases linearly with the height h and it is usually close to $h/2$. Inner scale typically presents values on the order of millimeters and, only at the high altitude, could reach the order of centimeters. For the Kolmogorov cascade theory, shown in Figure 1.4, large eddies reduce into smaller ones creating a continuous cascade from large to small scale size. This region is well known as *inertial range*. In the case of eddies size, smaller than l_0, we can consider a dissipation region (also known as dissipation range). The outer and inner scale are important parameters able to characterize the optical turbulence.

The refractive index structure parameter C_n^2, instead, permits to evaluate the optical turbulence strength. C_n^2 is commonly defined as a constant in the refractive index structure function D_n given by:

$$D_n(R) = \begin{cases} C_n^2 R^{2/3} & l_0 \ll R \ll L_o \\ C_n^2 l_o^{-4/3} R^2 & 0 \leq R \ll l_0 \end{cases} \quad (1)$$

where R is the scalar distance between two points in the space.

The values of C_n^2 are usually in the range $10^{-14} \div 10^{-12}$ [$m^{-2/3}$] close to the ground. Moreover the structure parameter changes with the height. Among the models able to describe the C_n^2, the Hufnagel-Valley (H-V) model is the most used one. C_n^2 variations can be calculated by the following expression:

$$C_n^2 = 0.00594\left(\frac{w}{27}\right)^2 (10^{-5}h)^{10} e^{\left(\frac{-h}{1000}\right)} + 2.7 \times 10^{-16} e^{\left(\frac{-h}{1500}\right)} + Ae^{\left(\frac{-h}{100}\right)} \quad (2)$$

where w is the rms wind speed [m/s] , h is the altitude [m] and A is the value of $C_n^2(0)$ [$m^{-2/3}$] at the ground. In particular, in this work, the H-$V_{5/7}$ [5,6] was employed, in which w = 21 m/s and $A = 1.7\times10^{-14}$ $m^{-2/3}$.

In the visible and near infrared regions, the refractive index fluctuations, due to the turbulence, depend mainly by the temperature variations [6]. In this case, we can obtain the C_n^2 with a different approach. It is reported in the following the expression of the temperature structure function [5]:

$$D_T(R) = \langle (T_1 - T_2)^2 \rangle = \begin{cases} C_T^2\, l_0^{-4/3}\, R^2, & 0 \le R \ll l_0 \\ C_T^2\, R^{2/3}, & l_o \ll R \ll L_0 \end{cases} \quad (3)$$

where

- T_1 and T_2 denote the temperature in Kelvin at two points separated by the distance R;
- C_T^2 is the *temperature structure constant* [$deg^2/m^{2/3}$];

By using the values of C_T^2 derived from the expression (3), we can calculate C_n^2 with the following relation [6]:

$$C_n^2 = \left(79 \times 10^{-6} \frac{P}{T^2}\right)^2 C_T^2 \quad (4)$$

where P is the pressure in millibars and T is the temperature in Kelvin.

Temperature gradient measurements permit to evaluate the C_n^2 of an air volume, as it will be described in Chapter 3.

A laser beam propagating through a turbulent medium is affected by irradiance fluctuations due to refractive index variations along its path. This phenomenon is known as scintillation. More in detail, in a propagation medium affected by thermal turbulence, random

cells, with variable sizes (10 cm – 1 km) and different temperatures, are generated. They present different refractive indices that cause scattering, multiple paths and angle-of-arrival variations. The scintillation intensity and its frequency depend on the size of the cells, and on the beam size. In particular, under scintillation, different parts of a laser beam travel along slightly different paths and then recombine. The recombination may be destructive or constructive, at any certain time, and results in recurring temporary signal losses. Of course, these irradiance fluctuations degrade the performance of the FSO system. When the heterogeneities are large, if compared to the beam cross section, the beam is deviated. Instead, when they are small, the beam expands. [19]. The scintillation is larger under hot sunshine (especially in the middle of the afternoon), when air is visibly shimmering, but it occurs at all the time, and for this reason the stars twinkle in the night sky. Another example of the scintillation effect is the mirage that appears as a lake in the middle of the hot asphalt.

The normalized variance σ_I^2 of the propagating optical beam intensity *I*, detected at the receiver, is termed *scintillation index* and offers an evaluation of the scintillation intensity. It is defined as [5,6]:

$$\sigma_I^2 = \frac{<I^2>-<I>^2}{<I>^2} = \frac{<I^2>}{<I>^2} - 1 \tag{5}$$

where *I* denotes the irradiance of the optical wave and the angle brackets < > denote an ensemble average. Another important parameter that offers a measure of the strength of the optical turbulence is the Rytov variance [5,6]. For plane wave propagation it is defined by the general expression [20]:

$$\sigma_R^2 = 0.56\, k^{7/6} \int_0^L C_n^2(x)(L-x)^{5/6}\, dx \tag{6}$$

where C_n^2 is the refractive index structure parameter, *k* is the wavenumber and *L* is the path length (distance from the transmitter to the receiver).

In the case of slant path, C_n^2 changes with the altitude, thus, the Rytov variance is given by the following expression:

$$\sigma_l^2 = 2.25\mu_1 k^{7/6}\left(H - h_0\right)^{5/6}\left[\sec(\zeta)\right]^{11/6} \tag{7}$$

where *k* is the wavenumber, *H* is the satellite altitude, h_0 is the ground station altitude, ς is the zenith angle, μ_1 is defined in Refs. [1, 2] and it is dependent on the refractive index structure

parameter C_n^2 [$m^{-2/3}$]. As already mentioned, the latter depends on the altitude, and in particular it is important for distances, from the ground-station, up to around 20 km. Over this altitude, C_n^2 can be considered negligible. The variations of the C_n^2 with the altitude are predicted with the Hufnagel-Valley model described by the expression (2) described above.

For terrestrial link (horizontal path) we can consider C_n^2 constant and, therefore, the Rytov variance reduces to:

$$\sigma_R^2 = 1.23 C_n^2 k^{7/6} L^{11/6} \tag{8}$$

where k is the wavenumber and L is the path length (distance from the transmitter to the receiver). In the case of point detectors, the relationship between the scintillation index and the Rytov variance is expressed by:

$$\sigma_I^2 \cong exp\left[\frac{0.49\sigma_R^2}{\left(1+1.11\sigma_R^{12/5}\right)^{7/6}} + \frac{0.51\sigma_R^2}{\left(1+0.69\sigma_R^{12/5}\right)^{5/6}}\right] - 1 \tag{9}$$

Figure 1.5 shows the scintillation index as a function of the Rytov variance. It is worth noting that the scintillation index increases linearly with the Rytov parameter -within the weak regime- and continues to increase to a maximum value greater than 1. As it reaches the maximum, it starts to decrease due to the multiple scattering that leads to self interference. Finally, it approaches again to 1, as the turbulence fading approaches the saturation regime.

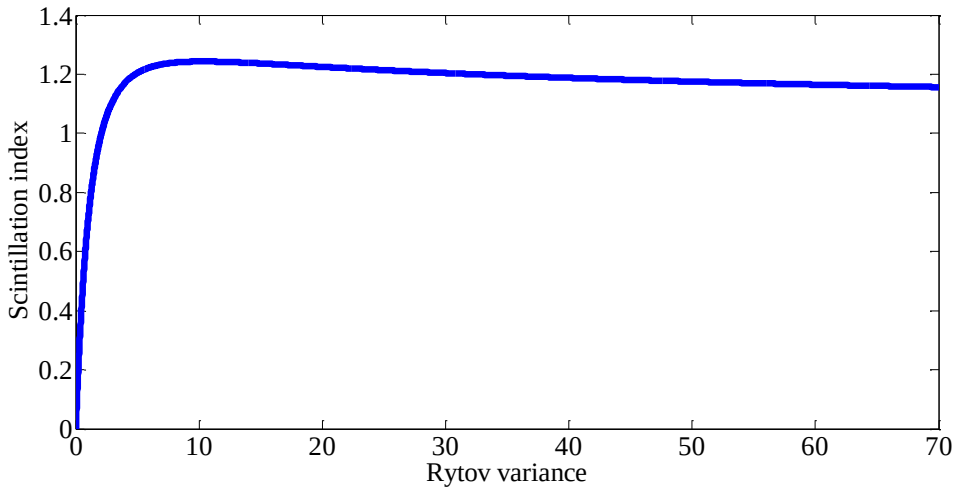

Figure 1.5 – σ_I^2 against log intensity variance for $C_n^2 = 10^{-15}$ $m^{-2/3}$ and $\lambda = 830$nm.

Large-scale sizes lead to the refraction of the optical wave, while small-scale sizes cause the wave to diffract. In general, the diffractive small-scale contribution to scintillation is caused by scale sizes smaller than the Fresnel zone $(L/k)^{1/2}$ or by the spatial coherence radius ρ_0, whichever is the smallest, while the refractive large-scale effect is caused by scale sizes larger than the Fresnel zone or by the scattering disk $L/k\,\rho_0$, whichever is the largest. For this reason, in the moderate-to-strong fluctuation regime, medium-sized eddies, smaller than the scattering disk and larger than the coherence radius, do not generate scintillation and will not contribute to the irradiance fluctuations [21].

If the collecting aperture diameter of an optical receiver is larger than the spatial scale of the optical scintillations, that are generated by atmospheric turbulence, the receiver will average fluctuations of the received waveform over the aperture area, thus reducing signal fluctuations. This phenomenon is known as *aperture averaging*.

Under weak irradiance fluctuations, the aperture averaging generally takes place when the radius of the collecting aperture is significantly larger than the Fresnel zone radius at the pupil plane of the detector lens. However, under strong irradiance fluctuations, the size of the collecting aperture radius determines whether the aperture averaging takes place or not. The scintillation index and the aperture averaging in the case of plane waves and of negligible inner/outer scale (i.e., *zero inner scale*) will be herein calculated [6].

The aperture averaging coefficient for an unbounded plane wave, in the absence of inner-scale/outer-scale effects, is defined by [5,6]:

$$A = \frac{\sigma_I^2(D)}{\sigma_I^2(0)} \tag{10}$$

where D [m] is the aperture diameter of the detector.

The scintillation index in the case of non-point detector is given by:

$$\sigma_I^2(D) \cong exp\left[\frac{0.49\sigma_R^2}{\left(1+0.65\,d^2+1.11\sigma_R^{12/5}\right)^{7/6}} + \frac{0.51\sigma_l^2\left(1+0.69\sigma_R^{12/5}\right)^{-5/6}}{1+0.90d^2+0.62d^2\sigma_R^{12/5}}\right] - 1 \tag{11}$$

where d is defined as follows:

$$d = \sqrt{\frac{kD^2}{4L}} \tag{12}$$

In weak conditions, that correspond to $\sigma_R^2(D)<1$, the coefficient A can be approximated by the interpolation formula [6]:

$$A = \left[1 + 1.06\left(\frac{kD^2}{4L}\right)\right]^{-7/6}, \qquad \sigma_R^2(D) < 1 \tag{13}$$

The effects of the aperture averaging in the relationship between the scintillation index and the Rytov variance is, substantially, a reduction of the maximum value of the scintillation index, that can be less than 1. In the measurement campaign that I have performed, and that will be described in Chapter 3, I have used the expression (5) to evaluate the scintillation index. However, under the hypotheses of plane wave propagation and zero inner scale, it is possible to extract the Rytov variance value from the expression (11) and, then calculate the aperture averaging coefficient using expressions (9) and (10).

References

[1] K. Tsukamoto, A. Hashimoto, Y. Aburakawa, and M. Matsumoto, “The Case for Free Space,” IEEE Microwave Magazine, vol. 10, no. 5, pp. 84 – 92, 2009.

[2] M. Toyoshima, "Trends in satellite communications and the role of optical free-space communications [Invited]", Journal of Optical Networking, vol. 4, pp.300 -311 2005.

[3] S. Arnon and D. Kedar, “Non line of sight underwater optical wireless communication network,” Journal of the Optical Society of America A, 26(3), 530–539, 2009.

[4] Lightpointe, “How to Designa Reliable FSO System,” Lightpointe White Paper Series, 2009.

[5] L. C. Andrews, R. L. Phillips, and C. Y. Hopen, “Laser Beam Propagation through Random Media,” SPIE Press, Bellingham, WA, 2nd edition, 2005.

[6] L. C. Andrews, R. L. Phillips, and C. Y. Hopen, “Laser Beam Scintillation with Applications,” SPIE Press, Bellingham, WA, 2001.

[7] A. García-Zambrana, C. Castillo-Vázquez, and B. Castillo-Vázquez, “Outage performance of MIMO FSO links over strong turbulence and misalignment fading channels,” Optics Express, vol. 19, no. 14, pp. 13480-13496, 2011.

[8] Z. Hajjarian, J. Fadlullah, and M. Kavehrad, “MIMO Free Space Optical Communications in Turbid and Turbulent Atmosphere,” Journal of Communications, vol. 4, no. 8, pp. 524-532, 2009.

[9] A. Z. Dodd, “The Essential Guide to Telecommunications,” Prentice Hall, 2012.

[10] B. Bing, “Ubiquitous Broadband Access Networks with Peer-to-Peer Application”, in“Evolving the Access Network”, International Engineering Consortium, Natl Communictions Forum, 2006.

[11] I. I. Kim, and M. Achour, “Free-space links address the last-mile problem,” website: www.laserfocusworld..com, 2001.

[12] K. Kazaura, K. Wakamori, M. Matsumoto, T. Higashino, K. Tsukamoto, and S. Komaki, "RoFSO: A universal platform for convergence of fiber and free-space optical communication networks," IEEE Communications Magazine, vol.48, no.2, pp.130-137, 2010.

[13] R. Ramirez-Iniguez, S. M. Idrus, and Z. Sun, “Optical Wireless Communications: IR for Wireless Connectivity”, CRC Press, Boca Raton, Florida (USA), 2008.

[14] R. Nebuloni and C. Capsoni, “Effect of Hydrometeor Scattering on Optical Wave Propagation Through the Atmosphere,” in Proceedings of the 5th European Conference on Antennas and Propagation (EuCAP 2011), pp. 2513-2517, Rome, Italy, 2011.

[15] M. Montopoli, F. S. Marzano, and G. Vulpiani, “Analysis and Synthesis of Raindrop Size Distribution Time Series From Disdrometer Data,” IEEE Transactions on Geoscience and Remote Sensing, vol. 46, no. 2, pp. 466-478, 2008.

[16] S. Mori, F. S. Marzano, F. Frezza, G.M.T. Beleffi, V. Carrozzo, A. Busacca, A. Andò, “Model analysis of hydrometeor scattering effects on free space near-infrared links,” in Proceedings of the International Workshop on Optical Wireless Communications (IWOW), pp. 1-3, 2012.

[17] S. V. Kartalopoulos, “Free Space Optical Networks for Ultra-Broad Band Services”, John Wiley & Sons, New York (USA), Aug. 2011.

[18] S. K. Friedlander, “Smoke, Dust, and Haze: Fundamentals of Aerosol Dynamics,” Oxford University Press, Second Edition, 2000.

[19] H. Sizun, and C. Boisrobert, *“Free-Space Optics: Propagation and Communication”*, ed. Hermes Science Publishing, 2006.

[20] F. S. Vetelino, C. Young, L. Andrews, and J. Recolons, “Aperture averaging effects on the probability density of irradiance fluctuations in moderate-to-strong turbulence”, Applied Optics, vol. 46, no. 11, pp. 2099-2108, 2007.

[21] S. Karp, R. M. Gagliardi, S. E. Moran, and L. B. Stotts, “Optical Channels: fibers, clouds, water and the atmosphere”, Plenum Press, New York, 1988.

Chapter 2

"Irradiance time-series generator for FSO links"

2.1 Introduction

In Chapter 1 has been presented an overview of Free Space Optics (FSO) communications. The advantages of this kind of optical communication typologies in the Next Generation Networks (NGN) has been described. Unfortunately, the FSO links own some impairments, mostly due to the communications medium, that usually depend on the terrestrial atmosphere. In fact, the weather conditions can deteriorate the FSO link quality, and, in some specific cases, can interrupt the communications. The rain and the fog could produce big losses along the optical path, and the sun, the wind and the humidity can produce optical turbulence generating optical signal distortions and fading. This thesis focuses on the optical turbulence effects and, mostly, on the communication degradations that occur in FSO links. As previously mentioned, the optical turbulence causes optical power fluctuations at the detector (effect that it is also known as "scintillation") that can increase the BER and, also introduce burst errors in the communications. Furthermore, these phenomena have a random behavior and, for this reason, are predictable only by means of statistical approaches.

In literature, optical turbulence effects were extensively studied and numerous irradiance distribution models (e.g., lognormal, Gamma-Gamma, and negative exponential models [1-5]) were developed for different optical turbulence conditions. Moreover, the functions and parameters of the optical turbulence, for different wave propagation hypotheses (plane, spherical and Gaussian waves), were well defined. However, the probability distributions and the statistical parameters (probability of fading, expected number of fading and mean fade time [4,5]) only offer a general quantification of the fading problems and, in some cases, they could be not sufficient to carry out a whole investigation on the FSO link performance. In fact, in order to study the performance of the fading mitigation techniques it

could be important to have specific information about the fading, in terms of depth, duration, and temporal position. In the following, two different channel models for FSO links (terrestrial and space to ground) are presented. They are able to generate irradiance time-series at the detector that permits to predict all the characteristics of a fading and, for this reason, represents a valid tool to evaluate the performance of the fading mitigation methods.

2.2 Irradiance time-series generator

The aim of an irradiance time-series generator is to produce a prediction of irradiance fluctuations at the receiver due to the optical turbulence. It should also give an estimation for a large range of turbulence conditions (from weak to strong) and at different link specifications, such as optical path, wavelength, link typology, etc. Furthermore, the generator should produce a time-series with a specific duration and time resolution, in order to be suitable for a large application range. The channel models that were implemented and that will be presented, offer all these features. They were built starting from the covariance functions, the probability distributions and the expressions already reported in literature [4,5].

In detail, the irradiance time-series have been generated temporally correlating a set of irradiance samples having a suitable probability density function (PDF), that will be introduced in the next section [6,7,8]. For the temporal correlation of the samples, I have used a spatial covariance function, converted into a time function, by using the Taylor "frozen eddies hypothesis" [4,5]. A suitable iterative algorithm [9], permits to carry out the correlation process. Therefore, from a N number of input irradiance samples, the algorithm is able to produce an irradiance-series of the same length (N) and with a fixed temporal covariance. By changing the number (N) of the samples and/or the sampling frequency, it is also possible to adjust the duration and the temporal resolution of the generated irradiance time-series. Hence, in this way, it is possible to produce time-series with the desired length and resolution.

A block scheme of the time-series generator is depicted in Figure 2.1. The block "one" produces the N irradiance samples with a specific probability distribution. Its inputs are the number of samples N and the Rytov variance (a parameter that, as described in Chapter 1, offers a measure of the strength of the optical turbulence). The block "two" produces the Fast Fourier Transform (FFT) of the irradiance temporal covariance. Its inputs are the link

specifications (wavelength, path length), the Rytov variance and the sampling frequency (for the FFT computation). The outputs of the blocks "one" and "two" represent the inputs for the block "three". The output of the block "three" is the irradiance time-series. It is worth noting that the inputs of the entire time-series generator correspond to the inputs of the block "one" and "two", whereas the output corresponds to the block "three" output.

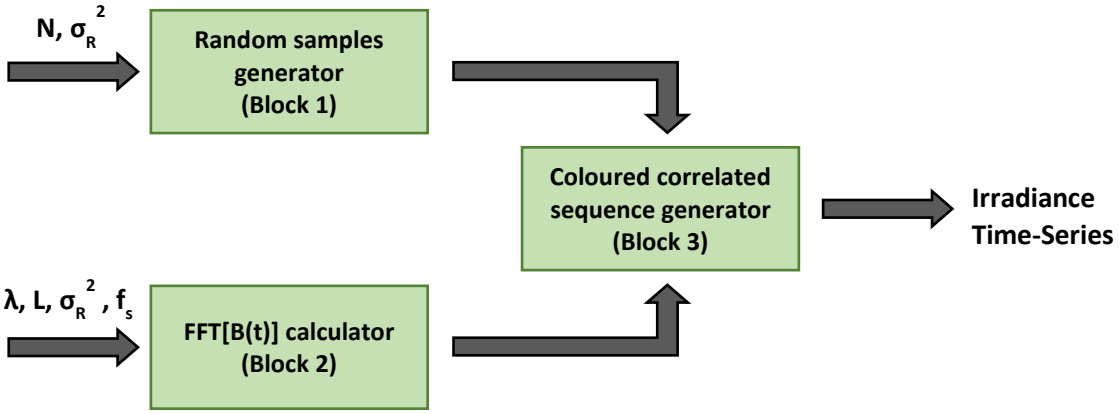

Figure 2.1 – Block scheme of the time-series generator

2.3 Probability Density Functions

Several distribution models (e.g., lognormal, negative exponential models, K-distribution) [1-5] were developed in literature to estimate optical turbulence effects in FSO communications links. In detail, the lognormal model is suitable for weak turbulence conditions, while negative exponential model is more appropriate for a very strong turbulence (i.e., saturate regime). Another model, which has provided excellent agreement with numerous experimental data, is the K-distribution. In particular, the latter is suitable under strong turbulence conditions, although an extension of this model also permits to cover weak fluctuation regimes (i.e., I-K distribution).

Instead, a more versatile model is the Gamma-Gamma PDF, which is able to estimate the optical turbulence (from weak to moderate-strong). This distribution is provided by two independent Gamma statistics which arise, respectively, from large-scale and small-scale atmospheric effects [4,5].

For the above-mentioned properties, the Gamma-Gamma PDF was employed in the irradiance time-series generator that has been implemented. However, at low values of the Rytov variance, it was not possible to compute some important parameters of the Gamma-Gamma distribution expression. For this reason, the lognormal PDF was used for very low values of the Rytov variance (σ_R^2 <0.014) (Section 1.4.1). Thanks to this choice, the irradiance time-series generator is able to cover a wide range of optical turbulence conditions.

In the following subsection, the details of the two PDFs, that were used in the channel model (lognormal and Gamma-Gamma), will be discussed.

2.3.1 Lognormal model

The lognormal distribution is a simple model for FSO communications providing the probability density of the optical irradiance values detected at the receiver. This model is generally valid only under weak fluctuations (σ_R^2<0.3) [4,5], where single optical wave scattering of the optical wave occurs, and it is described by the following PDF:

$$p(I) = \frac{1}{I\sqrt{2\pi\sigma_R^2}} exp\left(-\frac{\ln(I)-0.5\sigma_R^2}{2\sigma_R^2}\right) \quad (1)$$

where I is the irradiance normalized, with respect to the mean I_0.

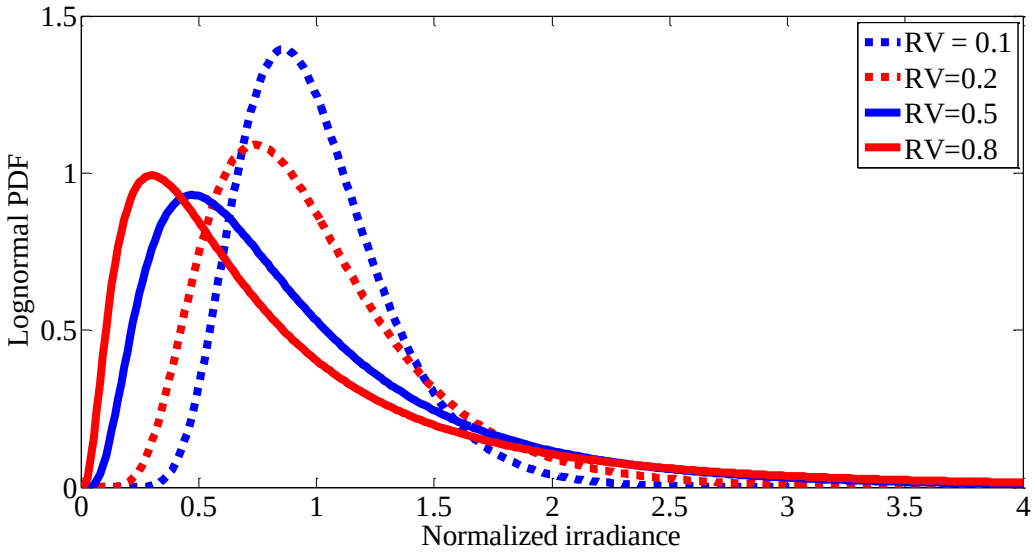

Figure 2.2 – Lognormal probability density function for a range Rytov variance (RV).

Figure 2.2 shows the lognormal PDFs for different values of σ_R^2. As it can be seen, at increasing Rytov variance, the expected value of irradiance decreases and the distribution becomes more skewed with longer tails towards infinity. This denotes the fluctuation extent of the irradiance as the channel inhomogeneity increases.

In order to obtain the lognormal turbulence model, the Rytov approximation has been used. According to this approximation, the Rytov parameter increases, without limit, as well as the refractive index structure parameter and/or the path length. As the turbulence strength increases beyond the weak regime, the turbulent eddies cause multiple scatterings that are not taken into account by Rytov in his approximation.

2.3.2 Gamma-Gamma model.

The Gamma-Gamma statistics is able to describe the FSO scintillation phenomena in a broad range of turbulence conditions and, for this reason, it is suitable to design our correlated model. The Gamma-Gamma model provides the PDF of received optical irradiance (I) in the following form:

$$p(I) = \frac{2(\alpha\beta)^{(\alpha+\beta)/2}}{\Gamma(\alpha)\Gamma(\beta)} I^{\{[(\alpha+\beta)/2]-1\}} K_{\alpha-\beta}\left(2\sqrt{\alpha\beta I}\right) \tag{2}$$

where I is the normalized irradiance $\Gamma(\cdot)$ is the Gamma function, $K_n(\cdot)$ is the modified Bessel function of the second kind of order n, while α and β are two parameters expressed, for plane wave propagation and at zero inner scale case [5], as follows:

$$\alpha = \left\{ \exp\left[\frac{0.49\sigma_R^{12/5}}{\left(1+1.11\sigma_R^{12/5}\right)^{7/6}} \right] - 1 \right\}^{-1} \tag{3}$$

$$\beta = \left\{ \exp\left[\frac{0.51\sigma_R^{12/5}}{\left(1+0.69\sigma_R^{12/5}\right)^{5/6}} \right] - 1 \right\}^{-1} \tag{4}$$

If compared to the lognormal distribution, the Gamma-Gamma distribution is a more versatile model which is able to estimate optical turbulence from weak to moderate-strong

fluctuation. In Figure 2.3 the Gamma-Gamma distribution for three different turbulence regimes (weak, moderate and strong) is depicted.

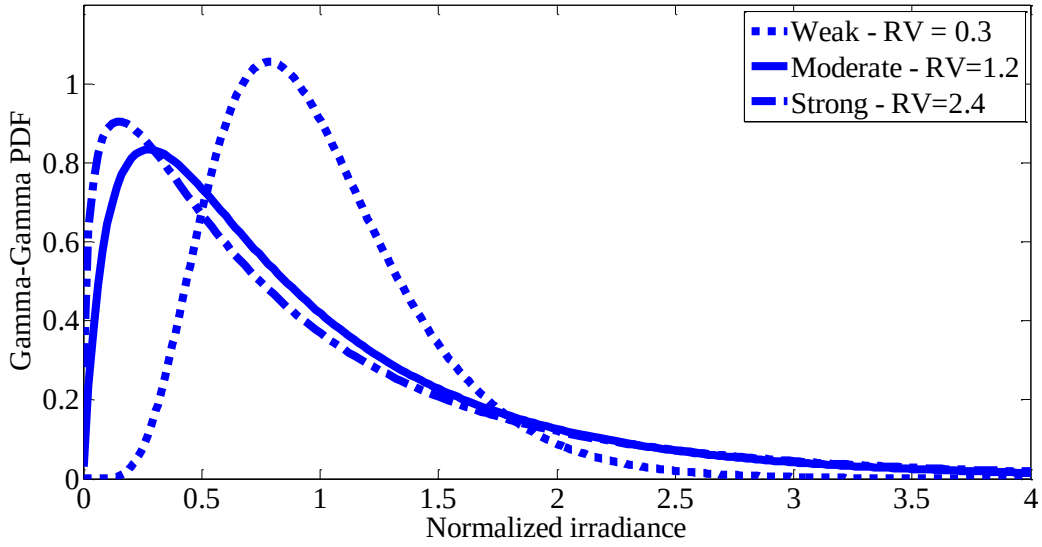

Figure 2.3 – Gamma-Gamma distribution for three different turbulence regimes: weak, moderate and strong (RV – Rytov variance).

2.4 Covariance functions

Starting from the probability density functions, it is possible to generate a random irradiance time-series, but it is mandatory to define a temporal correlation relationship between the samples. In the case of terrestrial links, assuming a plane-wave propagation, the spatial relationship -linking the optical irradiance values- is given by the following covariance function [4,5]:

$$B_I(\rho) = \exp\left[\left(\frac{0.49\sigma_R^2}{\left(1+1.11\sigma_R^{\frac{12}{5}}\right)^{\frac{7}{6}}}\right){}_1F_1\left(\frac{7}{6};1;-\frac{k(\rho)^2\eta_x}{4L}\right)+\left(\frac{0.50\sigma_R^2}{\left(1+0.69\sigma_R^{\frac{12}{5}}\right)^{\frac{5}{6}}}\right)\left(\frac{k(\rho)^2\eta_y}{L}\right)^{\frac{5}{12}}K_{5/6}\left(\sqrt{\frac{k(\rho)^2\eta_y}{L}}\right)\right]-1 \quad (5)$$

where ρ is the spatial variable, ${}_1F_1(\cdot)$ is the confluent hypergeometric function of the first kind, η_x and η_y are two parameters defined as follows [4,5]:

$$\eta_x = \frac{2.61}{1+1.11\sigma_R^{12/5}} \tag{6}$$

$$\eta_y = 3\left(1+0.69\sigma_R^{12/5}\right) \tag{7}$$

For the slant path, the irradiance covariance function is expressed as follows [4,5]:

$$B_I(\rho) = \exp\left\{\begin{array}{l}\sigma_{\ln(x)}^2\left[\mu_2(\rho)/\,\mu_2(0)\right]+ \\ +0.99\sigma_{\ln(y)}^2\left(\dfrac{k\rho^2\eta_y}{L}\right)^{5/12}K_{5/6}\left(\sqrt{\dfrac{k\rho^2\eta_y}{L}}\right)\end{array}\right\}-1 \tag{8}$$

where $\sigma^2_{ln\,(x)}$, $\sigma^2_{ln\,(y)}$ and η_y are parameters depending on the Rytov variance, while $\mu_2(\cdot)$ is a function of H, h_0 and C_n^2.

The previous expressions are function of spatial variable ρ. In order to convert the spatial covariance functions into time functions, I have applied the Taylor's "frozen eddies hypothesis" [4,5]. Under the latter hypothesis and considering the plane wave propagation, we can write the following:

$$\rho = vt \tag{9}$$

where t is the time and v is the average transverse wind speed (orthogonal to the propagation direction). Therefore, setting v in expression (8), and substituting it into (5), the covariance becomes a function of the only independent variable t.

2.5 Correlation algorithm

In order to carry out a prediction of irradiance fluctuations at different turbulence conditions, an irradiance time-series is generated, by means of the above-mentioned PDFs and temporal covariance expressions. Unfortunately, I have noticed that, when you try to correlate

a non-Gaussian distribution using only a correlation filter, the output distribution converges to a Gaussian one. Anyway, I have overcome this problem by means of a suitable algorithm [9], composed by a correlation filter and a nonlinear memoryless block function.

This algorithm is able to generate random processes with a defined marginal probability distribution and a power spectral density function (i.e., generating coloured, non-Gaussian signals). It is quite simple to implement, as it only involves the Fourier transform and a sorting routine. The correlation filter employed has been implemented using the Fourier amplitudes associated with the target power spectral density. The block function is memoryless, and this ensures that the spectral properties of the generated signal are not altered during the execution of the algorithm.

```
Algorithm I:
Sxx(N/2+1)=0; % zero out the DC component (remove mean)
Xf=sqrt(2*pi*N*Sxx/dt); % Convert PSD to Fourier amplitudes
Xf=ifftshift(Xf); % Put in Matlab FT format
x=raylrnd(1,[1,N]); % generate N iid samples conforming to p(x)
vs=(2*pi/N/dt)*sum(Sxx)*(N/(N-1)); % Get signal variance (as determined
by PSD)
x=x*sqrt(vs/var(x)); % guarantee new data match this variance
mx=mean(x); x=x-mx; % subtract the mean
[xo,indx]=sort(x); % store sorted signal xo with correct p(x)
k=1; indxp=zeros(1,N); % initialize counter
while(k)
Rk=fft(x); % Compute FT
Rp=atan2(imag(Rk),real(Rk)); % Get phases
x=real(ifft((exp(i.*Rp)).*abs(Xf))); % Give signal correct PSD
[zx,indx]=sort(x); % Get rank of signal with correct PSD
x(indx)=xo; % rank reorder (simulate nonlinear transform)
k=k+1; % increment counter
if(indx==indxp) k=0; end % if we converged, stop
indxp=indx; % re-set ordering for next iter
                                  end
x=x+mx; % Put back in the mean
```

Figure 2.4 – Algorithm to generate a colored correlate sequence [9].

In our case, the algorithm input parameters are: the double side Fourier Transform of the temporal irradiance covariance - obtained through the FFT of $B_I(t)$ - and a random irradiance samples sequence. The temporal spacing between two adjacent samples is the reciprocal of the FFT sampling frequency (f_c). This means that I can choose the temporal resolution of the sequence according to our needs. The details of the algorithm are depicted in Figure 2.4 [9].

In the following section, I will show some examples of the generated irradiance series for the terrestrial FSO link and for the satellite-to-ground downlink.

2.6 Irradiance time-series examples

In the previous sections the details of the irradiance time-series generator were described. The generator can predict irradiance fluctuations in terrestrial horizontal FSO links and, moreover, in satellite-to-ground FSO downlinks, where the plane wave propagation approximation is valid. In order to show all the tool features, in the next subsection, several examples of generated irradiance time-series are presented.

2.6.1 Terrestrial FSO links

Terrestrial FSO links usually cover horizontal path and, therefore, it is possible to consider the optical turbulence conditions constant (by means of the C_n^2) during the communications. However, in order to estimate the turbulence conditions, I have considered the Rytov variance, which can be computed knowing the wave number and the C_n^2. In my simulations. I have used a wavelength of 1550 nm that is widely used in the FSO communications and in fiber optics networks.

Another important parameter is the transverse wind speed (orthogonal to the optical signal direction), on which the correlation time of the irradiance fluctuations depends. In detail, with increasing transverse wind speed, the correlation time decreases and the bandwidth of the irradiance fluctuations grows. Finally, the FSO link specifications represent the other inputs of the time-series generator.

The time interval of the generated irradiance time-series depends on the values of the sampling frequency and the number of samples (N), and it is given by the following expression:

$$T = N/F_s \tag{10}$$

The generator I have implemented, uses a settable sampling frequency (F_s) and automatically computes the necessary number of samples. In the next examples, I have employed the sampling frequency of 100 kHz in order to have a temporal spacing of 10 μs. Of course, the sampling frequency can be set according to the needs and, usually, it is in the range

50÷1000 kHz. In these cases, the number of samples varies depending on the temporal covariance and the obtained time intervals are in the range 1÷100 s. Instead, the temporal spacing between two samples is given by the inverse of the sampling frequency.

In the next simulations, I have considered path lengths of 500 m and 1500 m, three different values of Rytov variance (0.1, 0.7 and 1.2), and three different values of the transverse wind speed. (0.1, 1 and 1 m/s). Furthermore, each irradiance time-series is normalized with respect to the irradiance mean value.

Figure 2.5 shows a portion of an irradiance time-series generated for σ_R^2 = 0.1, a sampling frequency of 100 kHz (temporal spacing of 10μs), and having a time interval of about 42 s. The generated time-series has a high temporal resolution, below a correlation time, that can be further improved, if desired, by increasing the sampling frequency.

Figure 2.6 depicts the comparison between the covariance function of the simulated irradiance fluctuations displayed in Figure 2.5 (dashed red line) and the input temporal covariance function (solid blue line). It is worth noting that the two above mentioned functions are very similar: so, the algorithm we used is able to properly correlate the irradiance samples.

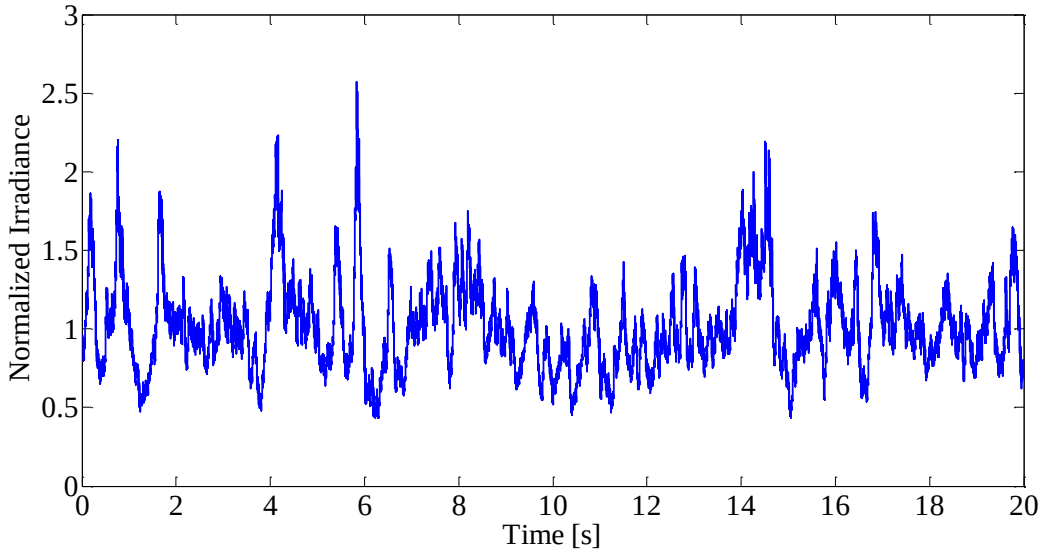

Figure 2.5 – Irradiance time-series for a Rytov variance σ_R^2=0.1, a transverse wind speed v=0.1m/s, and a sampling frequency f_s=100 kHz.

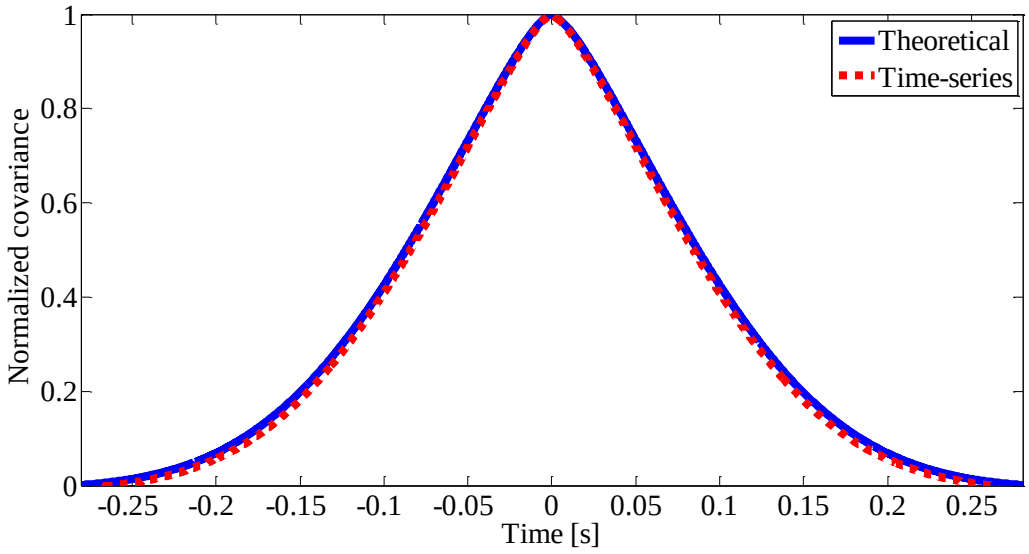

Figure 2.6 – Covariance functions of an irradiance time-series generated for a Rytov variance σ_R^2=0.1, a transverse wind speed v=0.1m/s, and a sampling frequency f_s=100 kHz.

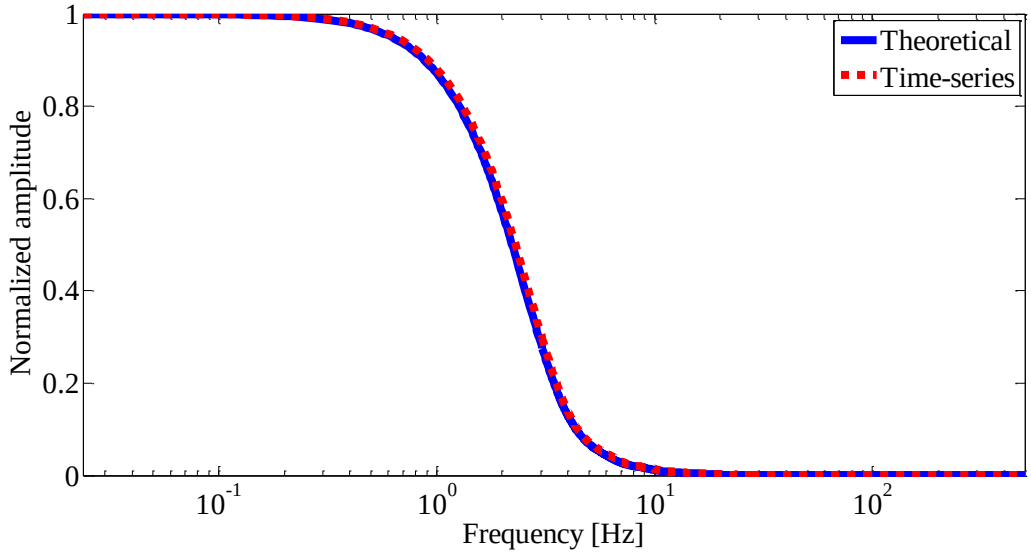

Figure 2.7 – Power spectral density of an irradiance time-series generated for a Rytov variance σ_R^2=0.1, a transverse wind speed v=0.1m/s, and a sampling frequency f_s=100 kHz.

Figure 2.7 depicts a comparison between the input theoretical power spectral density (solid blue line) and the power spectral density of the irradiance time-series (dashed red line). It is worth noting that, also for these characteristics, the time-series generator works well. Moreover, the spectral analyses highlight that the optical turbulence acts as a low-pass filter

behavior with, in this case, a 3dB bandwidth around 1.65 Hz. This is due to the low value of the transverse wind speed.

I have also analyzed the difference between the simulated irradiance fluctuations PDF and the Gamma-Gamma distribution. Figure 2.8 shows that both normalized PDFs are comparable. Therefore, the irradiance time series exhibits the correct probability density distribution.

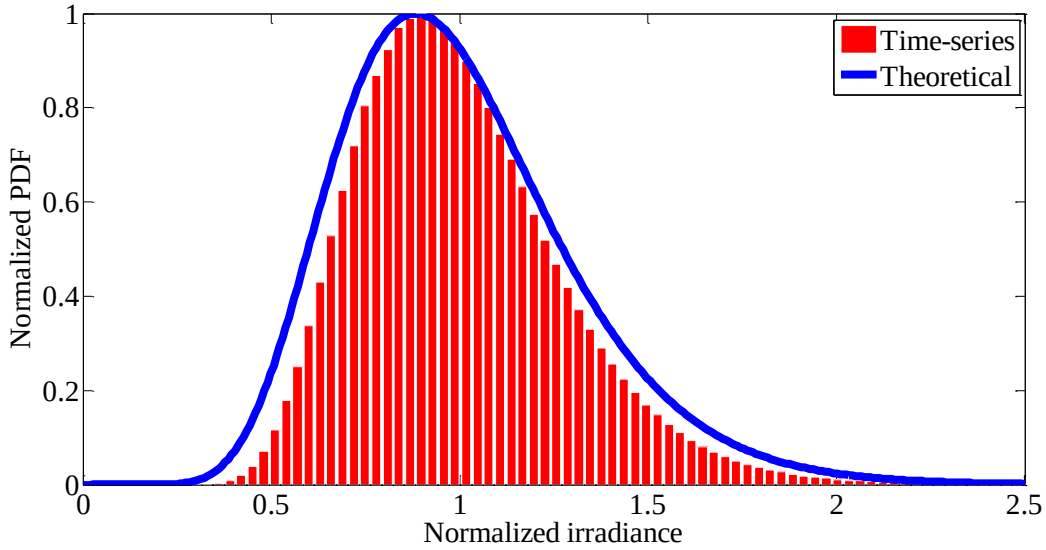

Figure 2.8 – Normalized histogram of an irradiance time-series generated for a Rytov variance σ_R^2=0.1, a transverse wind speed v=0.1m/s, and a sampling frequency fs=100 kHz, and the theoretical normalized probability density for the same value of Rytov variance.

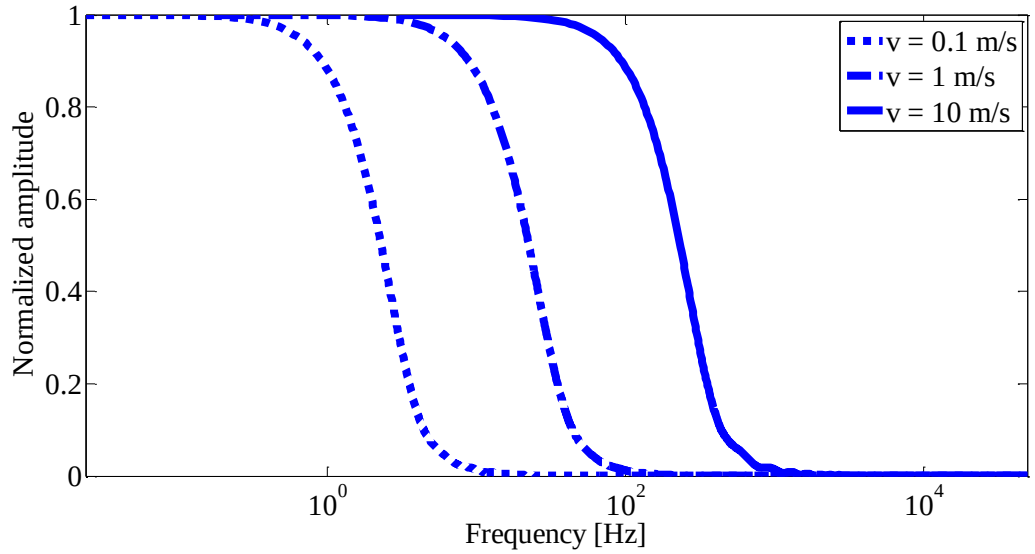

Figure 2.9 – Frequency spectrum of three different irradiance time-series generated for a Rytov variance σ_R^2=0.1, a sampling frequency f_s=100 kHz and for three different transverse wind speeds.

As previously mentioned, the bandwidth of the FSO channel depends on the transverse wind speed. In particular, when the latter increases, the correlation time decreases and the bandwidth of the channel grows. This behavior is explained with the Taylor frozen eddies hypothesis for the plane wave propagation (expression (9)) that introduces a linear relationship between the spatial variable ρ and time t. The irradiance generator, that I have implemented, uses this hypothesis and, thus, the produced time-series has these characteristics. Figure 2.9 shows a comparison of three different frequency spectra obtained from irradiance time-series generated for a 0.1 Rytov variance and at three different values of the transverse wind speed: 0.1, 1 and 10 m/s. For v=0.1 m/s the 3dB bandwidth is around 1.65 Hz, whereas for v=1 m/s and v=10 m/s 3dB bandwidths are, respectively, 16 Hz and 159 Hz. Therefore, bandwidth increases with v.

The examples I have shown, regard the weak optical turbulence conditions. Nevertheless, the Gamma-Gamma PDF is valid from weak to strong turbulence, so, the irradiance time-series generator is able to produce time-series even in the case of worse optical turbulence conditions.

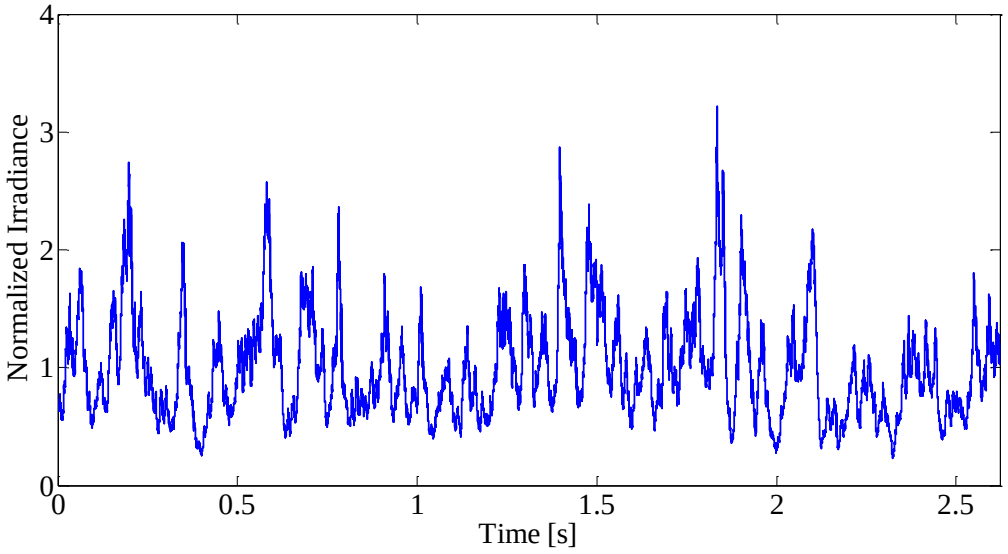

Figure 2.10 – Irradiance time-series for a Rytov variance σ_R^2=0.3, a transverse wind speed v=1m/s, a path length of 1500 m and a sampling frequency f_s=100 kHz.

Figures 2.10, 2.11 and 2.12 show three irradiance time-series generated at v=1 m/s and for a Rytov variance of 0.3, 0.7 and 1.2, respectively. The FSO link specifications I have considered, are: 1550 nm and a path length of 1500 m. It is worth noting that at

moderate/strong optical turbulence, the irradiance could assume values in a larger range, if compared to the case of weak turbulence. Moreover, the mean values of the irradiance decreases. In order to better highlight these differences, I have produced a graphical comparison (Figure 2.13) of the normalized distributions related to the irradiance time-series previously mentioned.

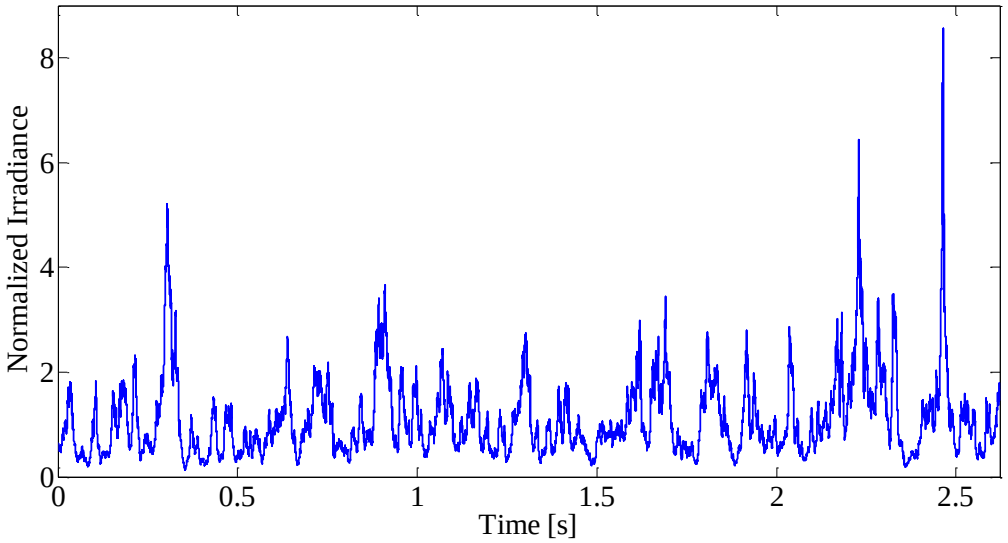

Figure 2.11 – Irradiance time-series for a Rytov variance σ_R^2=0.7, a transverse wind speed v=1m/s, a path length of 1500 m and a sampling frequency f_s=100 kHz.

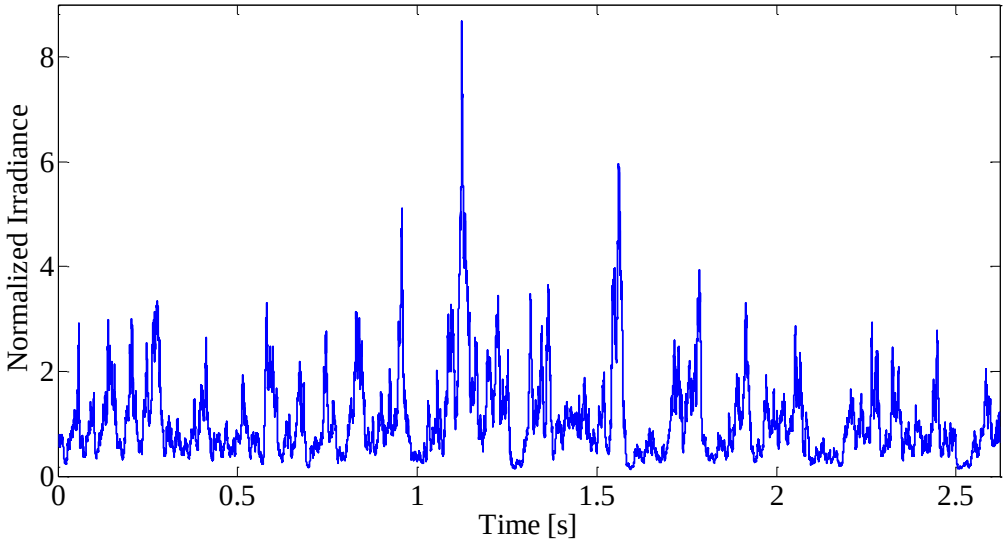

Figure 2.12 – Irradiance time-series for a Rytov variance σ_R^2=1.2, a transverse wind speed v=1m/s, a path length of 1500 m and a sampling frequency f_s=100 kHz.

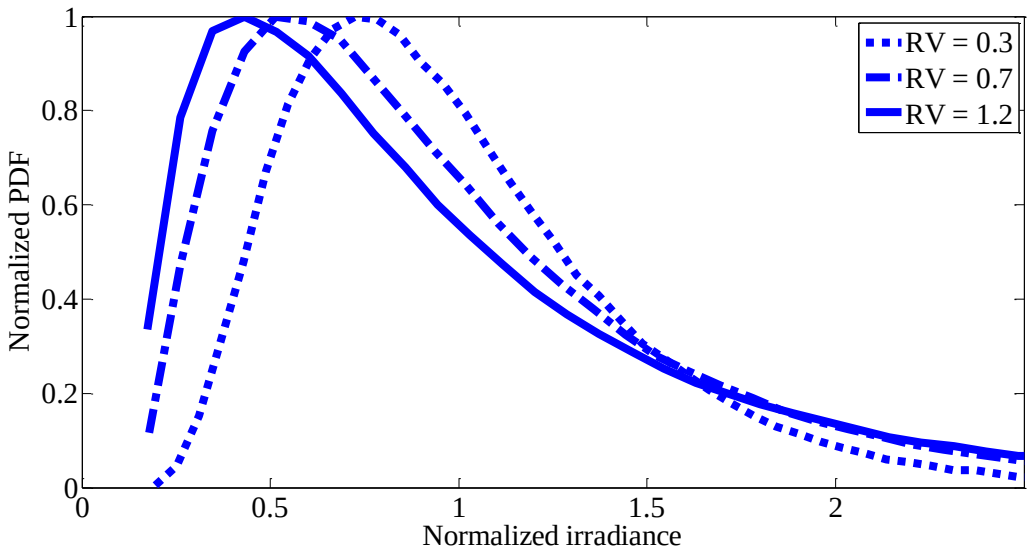

Figure 2.13 – Normalized histogram comparison of irradiance time-series generated for 0.3, 0.7 and 1.2 Rytov variance (σ_R^2), at a transverse wind speed v=1m/s, a path length of 1500 m and a sampling frequency f_s=100kHz.

From the PDF comparison, it is possible to derive that, at higher value of the Rytov variance, the expected values of the irradiance decrease and the tails of PDFs grow. This result confirm that a worsening of optical turbulence conditions causes an increase of irradiance fluctuations and, moreover, a reduction of the mean irradiance.

2.6.2 Satellite-to-ground downlinks

The FSO technology was introduced in space communications for the advantages that it offers: license free operation, high data rate transmission, electromagnetic immunity, etc. FSO links have been achieved for inter/intra satellite communications and also for satellite to ground communications. In this research, I have focused on the study of space to earth downlinks.

A satellite to ground FSO link is usually composed by a static ground station and, of course, a satellite that is located in a low orbit (LEO) or in a geostationary orbit (GEO). Unlike the terrestrial links, the optical path can be vertical or (more likely) slant, depending on the zenith angle that characterizes the link. Furthermore, the covered distance is largely greater than the terrestrial one, the optical turbulence conditions change along the path, the spatial coherence increases and the average transverse wind speed assumes high values. Long

distance links also involve more optical power (due to the losses) and a critical tracking procedure between the transmitter and the receiver.

Herein, I have generated some irradiance time-series related to a FSO downlink between a Geostationary Earth Orbit (GEO) satellite and a terrestrial ground station: the path length increases with the zenith angle, and consequently the optical turbulence effects augment at the receiver. Therefore, I have computed Rytov variance values for different zenith angles at the conditions summarized in Table 2.1. Results, reported in Table 2.2, show that the Rytov variance values are greater than 1 (under strong atmospheric turbulent conditions) at a zenith angle greater than or equal to around 73.8°, whereas, they are less than 1 (weak turbulence conditions) otherwise.

TABLE 2.1
RYTOV VARIANCE COMPUTATION PARAMETERS

Symbol	Quantity	Value
λ	Wavelength	1.06 μm
w	Wind speed	21 m/s
H	Satellite altitude	35800 km
h_0	Ground station altitude	0 m
A	C_n^2 at ground level	1.7×10^{-14} $m^{-2/3}$

TABLE 2.2
RYTOV VARIANCE AT DIFFERENT VALUES OF ZENITH ANGLE FOR A GEO SATELLITE TO GROUND LINK

Zenith Angles	Value
0°	0.09
30°	0.12
45°	0.18
60°	0.30
73.8	1.01
80°	2.4

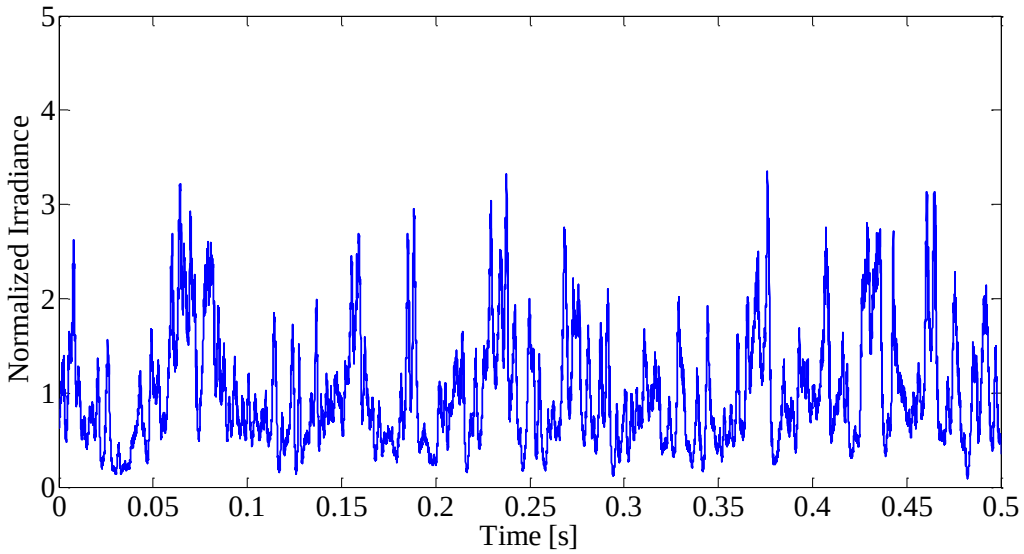

Figure 2.14 – Irradiance time-series for 60° zenith angle, at 1.06 μm wavelength, h_0=0 m, 0.2 s time interval and 10μs temporal spacing.

Figure 2.14 reports a portion of an irradiance time-series generated supposing 60° zenith angle (Rytov variance σ_R^2=0.7), an average transverse wind speed v=1m/s and a sampling frequency f_s=100 kHz. The other link parameters are reported in Table 2.1. Figure 2.15 shows a comparison between the theoretical input sample distribution (solid line) and the output one, as extracted from the irradiance generated time-series (dashed line). There is a good fit between the theoretical distribution and the generated time-series statistical distribution.

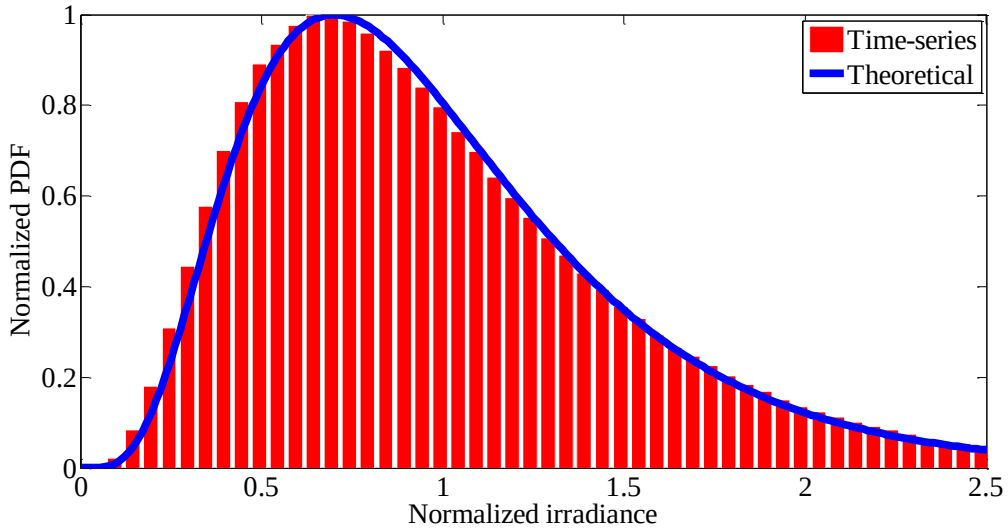

Figure 2.15 – Normalized probability density for 60° zenith angle, at 1.06 μm wavelength, h_0=0 m, 0.2 s time interval and 10μs temporal spacing.

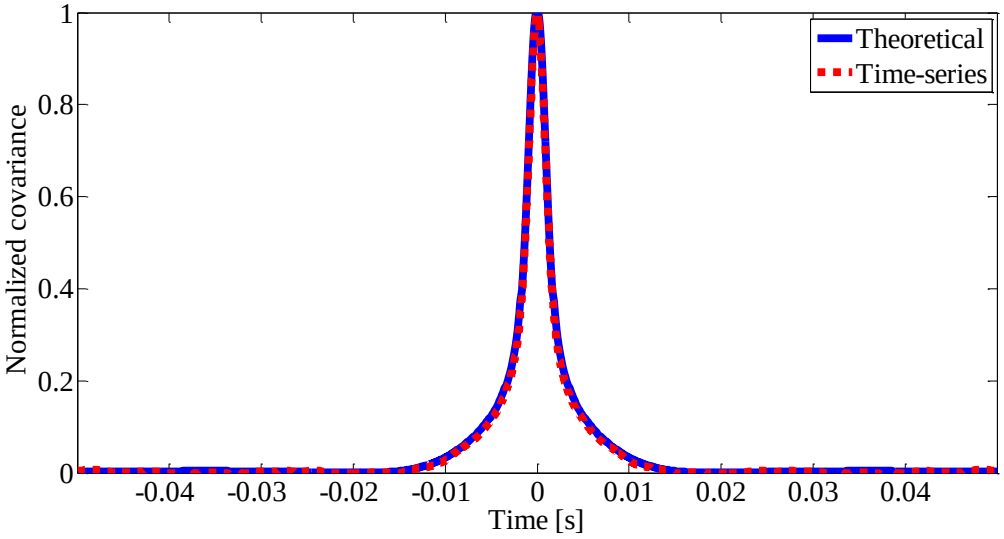

Figure 2.16 – Normalized irradiance temporal covariance for 60° zenith angle: theoretical and of the generated time series.

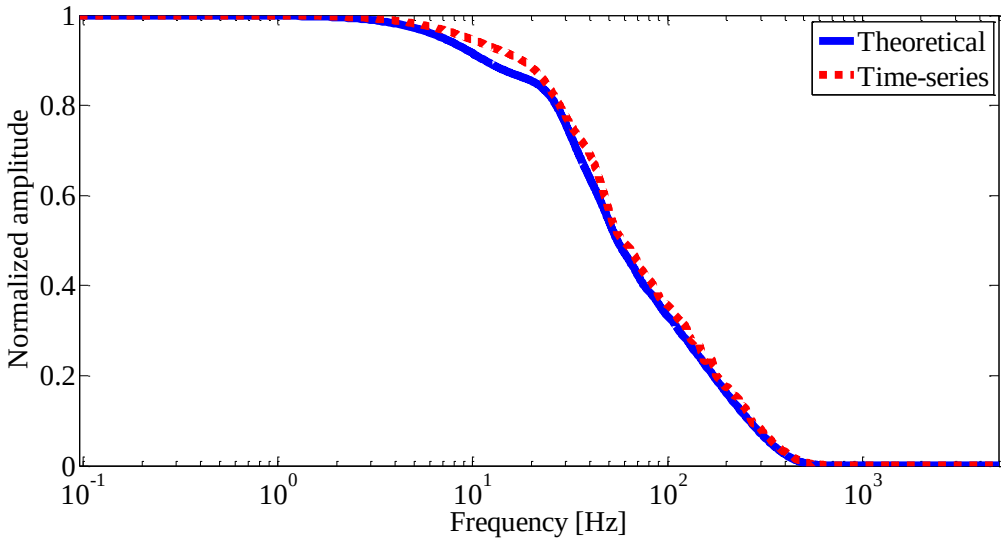

Figure 2.17 – Frequency spectrum for 60° zenith angle: theoretical and of the generated time series.

With regards to the temporal correlation, Figure 2.16 depicts a comparison between the theoretical input sample distribution (solid line) and the output one, as extracted from the irradiance time series (dashed line). The spectral analyses, shown in Figure 2.17, highlight that, in these optical turbulence conditions, the 3dB bandwidth of the FSO channel is around 30 Hz. Wider bandwidths occur at values of the transverse wind speed greater than 1 m/s.

Also in this case, all the diagrams show a good fitting between the theoretical input and the time-series functions. Hence, the channel I have implemented is able to predict, with a good approximation, temporal irradiance fluctuations at the receiver.

References

[1] S. Karp, R. M. Gagliardi, S. E. Moran, and L. B. Stotts, "Optical Channels: fibers, clouds, water and the atmosphere," Plenum Press, New York, 1988.

[2] G. R. Osche, "Optical Detection Theory for Laser Applications," Wiley, New Jersey, 2002.

[3] J. W. Goodman, "Statistical Optics ," Wiley, New York, 1985.

[4] A. Andò, S. Mangione, L. Curcio, S. Stivala, G. Garbo, R. Pernice, A.C. Busacca, "Recovery Capabilities of Rateless Codes on Simulated Turbulent Terrestrial Free Space Optics Channel Model," International Journal of Antennas and Propagation, Article ID 692915, 2013.

[5] A. Andò, S. Mangione, L. Curcio, S. Stivala, G. Garbo, A. Busacca, G. M. Tosi Beleffi, F. S. Marzano, "Rateless codes Performance tests on terrestrial FSO time-correlated channel model," in Proceeding IEEE of the International Workshop on Optical Wireless (IWOW), pp 1-3, 2012.

[6] A. Andò, G. Messineo, L. Curcio, S. Mangione, P. Gallo, A. C. Busacca, "Rateless codes performance analysis in correlated channel model for GEO Free Space Optics downlinks," in Proceeding IEEE of the International Conference on Space Optical Systems and applications, 2012.

[7] L. C. Andrews, R. L. Phillips, and C. Y. Hopen, "Laser Beam Propagation through Random Media," SPIE Press, Bellingham, WA, 2nd edition, 2005.

[8] L. C. Andrews, R. L. Phillips, and C. Y. Hopen, "Laser Beam Scintillation with Applications," SPIE Press, Bellingham, WA, 2001.

[9] J.M. Nichols, C.C. Olson, J.V. Michalowicz, and F. Bucholtz, “A simple algorithm for generating spectrally colored, non-Gaussian signals,” Probabilistic Engineering Mechanics, vol. 25, no. 3, pp. 315-322, 2010.

Chapter 3

"Measurements and model verification"

3.1 Introduction

I have carried out several measurement campaigns in order to investigate the performance of the FSO links affected by optical turbulence, and also collected several experimental data to characterize the optical power fluctuations due to the scintillation. Moreover, I have compared some experimental measurements, with the irradiance time-series generated by the generator, for the horizontal FSO links that have described in Chapter 2.

The measurement campaigns were performed at the University of Palermo, using the Laboratory of Optics of the Department of Energy Information engineering and Mathematical models (DEIM), and at the Northumbria University (Newcastle - UK) in the well-equipped Laboratory of Optics of the Optical Communications Research Group.

3.2 Measurements in the University of Palermo

In order to examine the validity of the developed channel model, I have set up, in our optical laboratory, a short FSO link, 2.70 m long, where I have induced turbulence via a fan heater.

The measurement set-up, shown in Figure 3.1, is composed of a 1550 nm laser diode connected to a single mode fiber, a fiber collimator, two planar mirrors and a germanium photodiode as a detector. Each component was placed on an optical table, in order to reduce the area involved in the turbulences produced by the fan heater. I have also used an infrared filter to reduce the environmental noise.

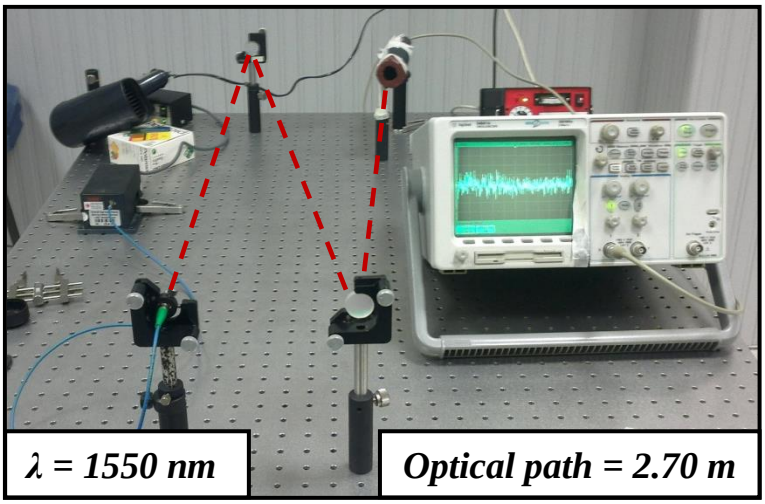

Figure 3.1 – Measurement set-up for power fluctuations caused by the turbulence produced by a fan heater.

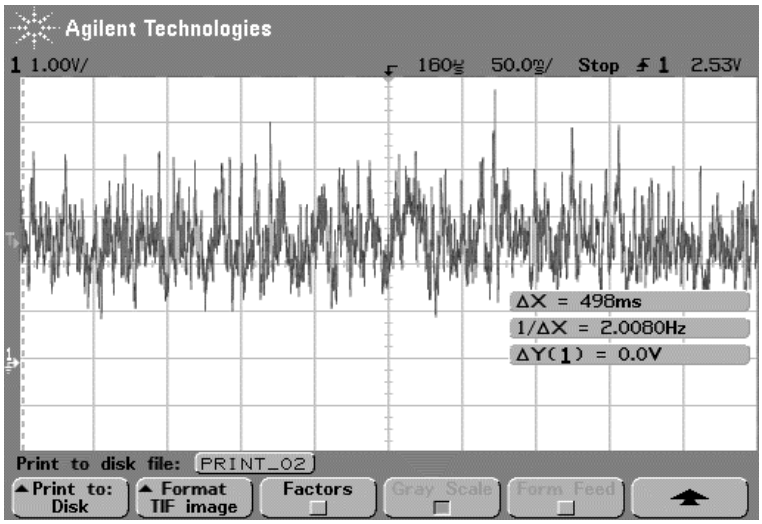

Figure 3.2 – Oscilloscope screenshot of power fluctuations taken for a 1550 nm laser in free space propagation detected with a germanium photodiode.

The fiber-coupled laser diode was able to provide a variable output optical power with a maximum value of 1 mW. Its output connector (FC-APC) was plugged to a fiber collimator, which allowed us to modify the diameter of the laser spot at the detector. The two mirrors allowed us to fix the optical path at 2.70 m, and the mirrors also permitted to accurately point the beam into the detector.

I have set up the fiber collimator and the power of the laser so that the laser spot was bigger than the detector size (the detector can be considered as a point detector, and, hence, the plane wave approximation is valid) with a maximum detected signal voltage of around 2 V. The input impedance of the oscilloscope was set to 1 MΩ.

Figure 3.2 shows an example of the measured power fluctuations acquired by the described measurement system. It is worth noting that fluctuations of about 1 V, around the mean voltage value, were observed.

By means of the previous measurements and of the following expression of the scintillation index [1,2]:

$$\sigma_I^2 = \frac{\langle I^2 \rangle}{\langle I \rangle^2} - 1 \tag{1}$$

where < > is the average and I is the irradiance, we found a value of the scintillation index that it was equal to 0.05. This value corresponds to weak turbulence conditions, so we can assume that the values of the scintillation index and the Rytov variance are similar [1,2].

Irradiance time-series, displayed in Figure 3.3, has been generated using the experimental FSO link specifications and the Rytov variance value obtained from the measurements.

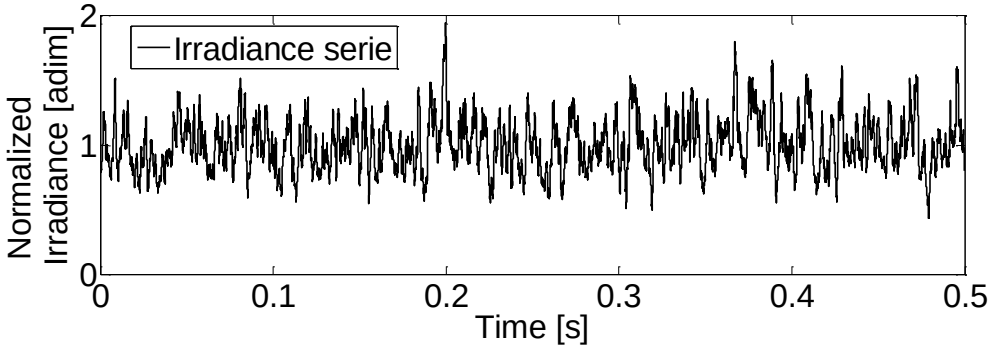

Figure 3.3 – Irradiance time-series generated with the parameters corresponding to the measurement conditions.

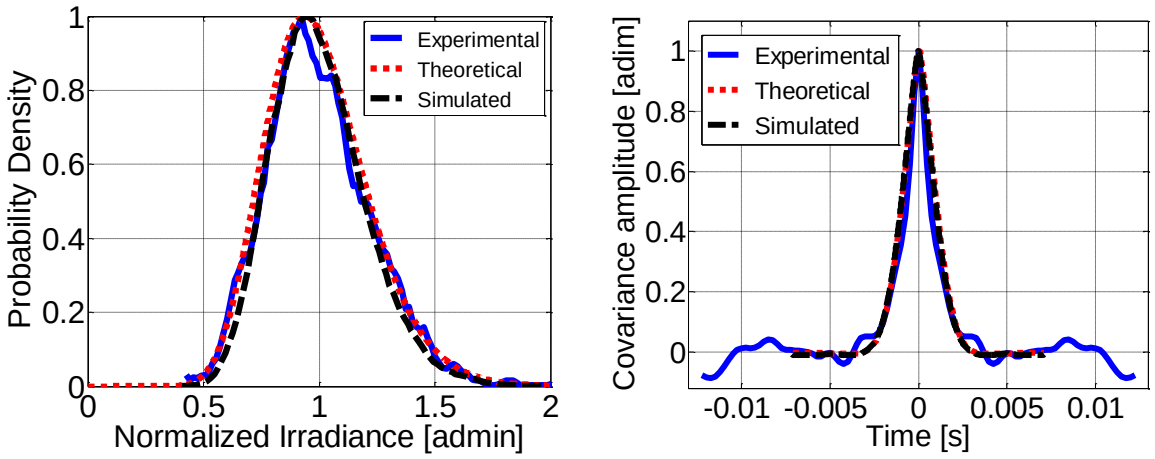

Figure 3.4 – Covariance and Probability distribution comparisons.

The probability distribution and the temporal covariance have been collected in the case of experimental, theoretical and the above mentioned irradiance series. With regard to the temporal covariance, I have considered a 0.7 m/s transverse wind speed .

In Figure 3.4 the normalized probability density and the normalized irradiance covariance are shown. A comparison of the experimental, theoretical and predicted data (obtained via my time correlated channel model) is shown. It is worth noting that the all three curves present a good fitting. This means that our channel model is valid for weak turbulence conditions.

3.3 Measurements in the Northumbria University

I have performed a wide measurement campaign in the Optical Laboratory of the Optical Communications Research Group (OCRG). In this laboratory, I had the chance to use several suitable equipments for FSO communications and also two different environmentally controlled chambers, which allowed me to generate several turbulence conditions.

3.3.1 Measurements set-up

As mentioned for the experimental measurements that were performed in the Optical Laboratory of OCRG (University of Northumbria), I have used two different chambers: one

indoor atmospheric and a controlled oven. For each chamber I have set up an experimental horizontal FSO link.

Figure 3.5 – Indoor atmospheric chamber – Optical Laboratory of Northumbria University.

Figure 3.5 shows the indoor atmospheric chamber [3,4,5]. It is made of glass and its dimensions are 5.5×0.3×0.3 m^3. It is composed of seven compartments, each one having a side hole that allows the air circulation along its length.

These features permit to perform a good temperature control in the chamber. Furthermore, hot-plates with built-in fans and thermometers were positioned inside the chamber. In order to create several turbulence conditions, external heaters were used to pump air (hot or cool, according to the needs) into the chamber. In this way, the temperature inside the chamber was able to reach values up to 50-60°C.

The temperature was continuously monitored: three temperature sensors were placed along the chamber at a fixed distance from each other (around 2.4 meters). Two anemometers were also employed to measure the wind speed close to the external heaters. At the receiver side, I have used a silicon PIN photodetector owning an integrated trans-impedance amplifier (TIA) that permits to reduce the noise and amplify the signal output of the photodetector. On

the transmitter side, I have employed a solid state laser with the following technical specifications: 830 nm emission wavelength, 10 mW power, class 3B. For the laser bias, a power supply providing 8÷12 V and 40÷70 mA was employed. The maximum laser modulation signal was 500 mV_{pp}. Moreover, a waveform generator (WFG) was used to produce the input data and a high-frequency Digital Storage Oscilloscope (DSO) was employed to display and acquire the input and output signals. Table 3.1 illustrates the technical specifications of the above mentioned equipment.

Equipment	Parameter	value
TRANSMITTER		
Function Generator	Manufacturer	Techtronics
	Model	AFG 3252
	Bandwidth	240 MHz
	Sampling Rate	2 GS/s
Laser Diode	Peak wavelength	830 nm
	Maximum optical power	10 mW
	Class	3B
	Laser beam propagation model	Plane
	Modulation Bandwidth	75 MHz
Channel	Dimension	5.5 × 0.3 × 0.3 m
	Temperature range	20-65 °C
RECEIVER		
Photodetector	Manufacturer	Thorlabs
	Model	PDA10A-EC
	Detector	Silicon PIN
	Active Area	0.8 mm^2
	Wavelength range	350 to 1100 nm
DSO	Manufacturer	Agilent Technologies
	Model	Infiniium DSO 9254A
	Analog Bandwidth	2.5 GHz
	Analog sample rate	20 GS/s (for 2 channels)

Table 3.1 – Equipment technical specifications

Figure 3.6 – FSO channel composed by a temperature-controlled oven and an air pump.

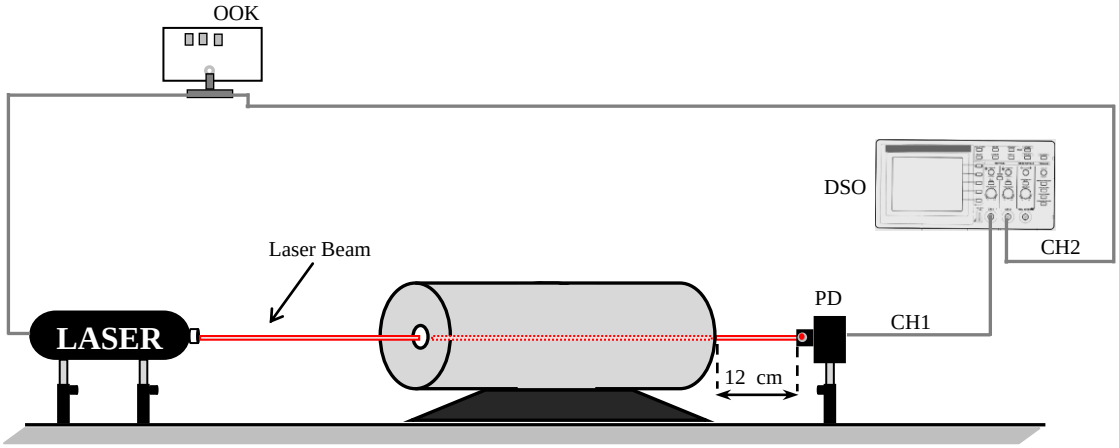

Figure 3.7 – Scheme of FSO channel composed by the oven and the air pump.

In addition to the above-mentioned test environment, a second measurement set-up was used. In this case, the turbulent FSO channel is composed of a temperature-controlled oven, 0.8-meter long, and an air pump (Figure 3.6). The latter blows cold air inside the oven that was able to heat up to 1200°C. As depicted in the scheme of Figure 3.7, the optical beam, produced by the laser, goes through the oven and is detected by the PIN diode placed at the output of the oven. The FSO link has a path length of around 1m. During all the

measurements, the temperature was constantly monitored by a thermal sensor placed inside the chamber.

Each measurement set-up requires different settings that will be described in the next section.

3.3.2 Measurement settings

The purpose of the measurement campaign was to calculate some important parameters (i.e., the eye-diagram, the Q-factor, and the BER), in order to evaluate the FSO link performance, at several different turbulence conditions created inside the laboratory chamber. During all the measurements, an OOK-NRZ modulation at several data rates was used.

For the indoor atmospheric chamber set-up, the measurement procedure is described in the following. First of all, an arbitrary waveform was loaded into the WFG generator, and, for each measurement, I have set-up the desired rate of OOK-NRZ modulation (1, 5 or 10 Mbps). At the same time, the proper configuration of the DSO was selected in order to take 20 samples/bit. For each rate, a thermal gradient inside the chamber was generated by turning on one of the three fan heaters. Later, for each measurement, the temperature inside the chamber was measured by using three different thermometers; in addition, both the input and the received signals were displayed on the DSO and then saved in a Comma Separated Values (CSV) file. The thermometers were placed at a distance of 2.4 meters each other. The detailed sketch of the measurement set-up is illustrated in Figure 3.8, while the distances between the instruments are detailed in Table 3.2. Measurement conditions are summarized in Table 3.3.
Also, for the second measurement set-up, before starting the measurements, the saved pattern was loaded into the waveform generator and a 400 mV_{pp} signal was selected. For each measurement, the desired rate of OOK-NRZ modulation (1, 5 or 10 Mbps) was set. In fact, at each cycle, the WFG sent 1000 bits, so I have set a frequency of 1 kHz, 5 kHz and 10 kHz to have an output data rate of 1 Mbps, 5 Mbps, and 10 Mbps, respectively. Moreover, during all the measurements, the temperature was constantly monitored by a thermal sensor placed inside the chamber.

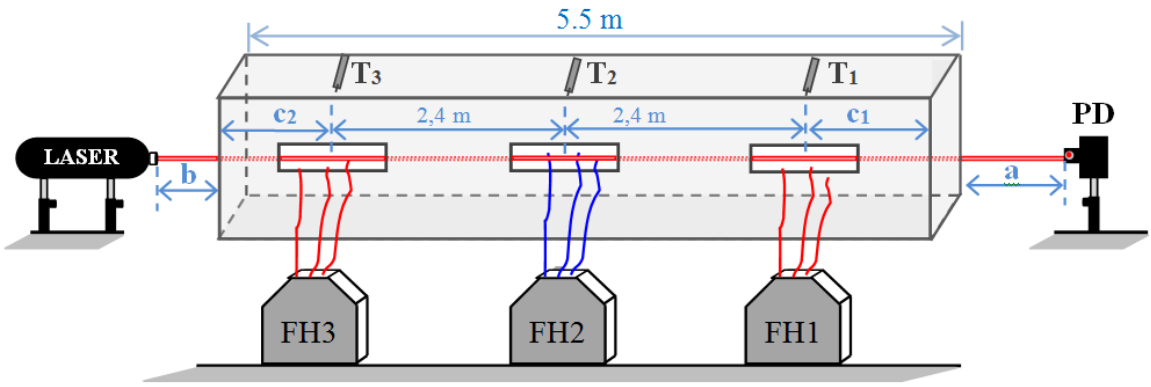

Figure 3.8 – Detailed sketch of the chamber set-up, with the relative position of each apparatus

Lengths	Values
a	0.33 m
b	0.24 m
c_1	0.35 m
c_2	0.35 m

Table 3.2 – Distances between the instruments

As already said, with regard to the other measurement setups, a 10 mW laser at 830 nm and a silicon photodetector PDA10A-EC were employed. After turning on the oven, it reached the steady temperature in a few minutes. The internal temperature of the oven, measured by a thermal sensor, was around 160 °C. The output of the WFG was sent to the laser and also, at the same time, directly to the oscilloscope through a coaxial cable. The output of the photodetector was connected to the channel 1 of the DSO, whereas the output of the WFG was connected to the channel 2. First of all, a rate of 1 Mbps was selected, and then the waveforms of both channels were acquired by the oscilloscope. Unlike the previous measurements, where the AC coupling mode was used, during these measurements the DC coupling mode was set on the DSO. The measurements at 5 Mbps and 10 Mbps were performed in the same way. Table 3.4 summarizes all the measurement conditions.

N° of measurement	Rate (Mbps)	Fan heater 1	Fan heater 2	Fan heater 3	Vin_{pp} (mV)	T1 (°C)	T2 (°C)	T3 (°C)
1	1	OFF	OFF	OFF	400	22	22	21
2	1	OFF	OFF	ON	400	23	25	35
3	1	OFF	OFF	ON	400	25	31	47
4	5	OFF	OFF	OFF	400	24	26	26
5	5	OFF	OFF	ON	400	24	28	35
6	5	OFF	OFF	ON	400	26	32	50
7	10	OFF	OFF	OFF	400	25	27	26
8	10	OFF	OFF	ON	400	25	26	25
9	10	OFF	OFF	ON	400	25	28	33
10	10	OFF	OFF	ON	400	28	36	47
11	1	OFF	OFF	OFF	400	25	28	26
12	1	ON	OFF	OFF	400	50	33	26
13	5	OFF	OFF	OFF	400	29	27	25
14	5	ON	OFF	OFF	400	33	28	25
15	5	ON	OFF	OFF	400	46	33	28
16	10	OFF	OFF	OFF	400	28	27	25
17	10	ON	OFF	OFF	400	36	29	25
18	10	ON	OFF	OFF	400	49	32	26

Table 3.3 – Measurement conditions (chamber)

N° of measure	Rate (Mbps)	Fan heater status	Vin_{pp} (mV)	Temperature(°C)
1	1	OFF	400	160
2	1	ON	400	160
3	5	OFF	400	162
4	5	ON	400	162
5	10	ON	400	154
6	10	OFF	400	162

Table 3.4 – Measurement conditions (oven)

3.3.3 Results

In the following section, I will describe and discuss the results of the whole measurement campaign carried out at the Northumbria University by using the set-up and the procedures previously illustrated.

It is worth noting that I have obtained the following results only afterward a necessary post-processing phase. In detail, I have filtered the received signals with a Butterworth filter of order 2. I have isolated the signal fluctuations due to the optical turbulence using point-by-point averaging operations. In order to compute the parameters related to the optical turbulence, I have considered the aperture averaging effects due to the size of the detector. Moreover, I have evaluated the performance of the FSO link under several conditions, computing also the Q-factor and the Bit Error Rate.

3.3.3.1 Indoor atmospheric Chamber set-up measurements

In the Table 3.5, the results of the measurement campaign, related to the set-up, using the indoor atmospheric chamber are shown. As already explained before, measurements at varying data rates (1, 5 and 10 Mbps) were performed. For each data rate, three kinds of measurement have been carried out: by taking all the fan heaters (FH) off, by turning ON the

fan heater positioned close to the receiver (*turb1* cases), by turning ON the fan heater positioned close to the transmitter (*turb3* cases). For each turbulence condition, two different measurements have been taken: the first was taken as the temperature, in the considered compartment of the chamber, has reached the value of 30-35 °C, and the second when the temperature has reached the value of 45-50°C.

Measure	Q_factor	BER	SI	Rytov variance	SI(0)	Aperture Averaging
OOK_01Mbps_turb1_25deg	47.6431	0.00E+00	0.000028	0.000036	0.000036	0.77336
OOK_01Mbps_turb1_50deg	3.9082	4.65E-05	0.004279	0.005531	0.005537	0.77292
OOK_01Mbps_turb3_35deg	1.8083	3.53E-02	0.042807	0.055723	0.055649	0.76923
OOK_01Mbps_turb3_47deg	3.1815	7.33E-04	0.007435	0.009611	0.009623	0.77261
OOK_05Mbps_turb1_29deg	50.0256	0.00E+00	0.000025	0.000032	0.000032	0.77336
OOK_05Mbps_turb1_33deg	8.2345	9.01E-17	0.000964	0.001246	0.001246	0.77326
OOK_05Mbps_turb1_46deg	7.4985	3.23E-14	0.001171	0.001514	0.001514	0.77324
OOK_05Mbps_turb3_26deg	29.8253	9.19E-196	0.000070	0.000091	0.000091	0.77336
OOK_05Mbps_turb3_35deg	3.3743	3.70E-04	0.005872	0.007591	0.007599	0.77277
OOK_05Mbps_turb3_50deg	2.5462	5.45E-03	0.009998	0.012927	0.012945	0.77236
OOK_10Mbps_turb1_28deg	21.2896	7.08E-101	0.000138	0.000179	0.000179	0.77335
OOK_10Mbps_turb1_36deg	3.2157	6.51E-04	0.006235	0.008059	0.008069	0.77273
OOK_10Mbps_turb1_49deg	4.9918	2.99E-07	0.002589	0.003347	0.003349	0.77309
OOK_10Mbps_turb3_25deg	21.2232	2.91E-100	0.000139	0.00018	0.00018	0.77335
OOK_10Mbps_turb3_33deg	1.4508	7.34E-02	0.07283	0.095804	0.095032	0.76637
OOK_10Mbps_turb3_47deg	2.0897	1.83E-02	0.015774	0.020408	0.020438	0.7718

Table 3.5 – Measurement results obtained using the “Chamber” set-up.

In detail, it was possible to observe that, when the fan heater positioned close to the transmitter was ON, higher values of turbulence were present. Instead, lower values of turbulence were reached turning ON the heater positioned close to the receiver. The complete results are shown in Table 3.5, while the complete measurement conditions have already been presented in the section 3.3.2, in the Table 3.3. I have obtained, in all the experiments, an aperture averaging of around 0.77.

The higher value of the scintillation index was σ_I^2=0.07283, therefore we were in a weak turbulence condition. Herein, I will discuss the most significant measurements, among the different turbulence cases (*turb1*, *turb3* and *noturb* – when no turbulence effects were induced in the FSO link), that it will be explained later, thus analyzing all the parameters and the obtained graphs.

Experiment 1

Measurement conditions:

- Data rate: 10 Mbps;
- Only the fan heater close to the receiver ON : FH1 = ON; FH2 = OFF; FH3 = OFF;

The first measurement was taken just after turning ON the FH1, therefore the temperature along the chamber was almost the same (equal to the room temperature). In particular, T1=28°C, T2= 27°C, T3=25°C. Therefore, this can be considered a "no turbulence" case, since the hot air being pumped inside the chamber was not able to generate any turbulence yet.

Figure 3.9(a) shows the signal received by the photodetector. The red circles represent the sampling points that permit to obtain the maximum value of the Q-factor.

Figure 3.9(b) illustrates the down-sampled signal (blue lines). In this case, the red line corresponds to the point-by-point average. In this way, it is possible to isolate the signal fluctuations due to the optical turbulence from the modulation. As it can be seen, there are no significant fluctuations of the received signal, this because negligible turbulence effects occur inside the chamber. The absence of turbulence is confirmed by the very low value of the obtained scintillation index (σ_I^2=0.000138), whereas the good quality of the link is shown by a high *Q*-factor value (Q = 21.2896) and the low BER (BER ≈ 0).

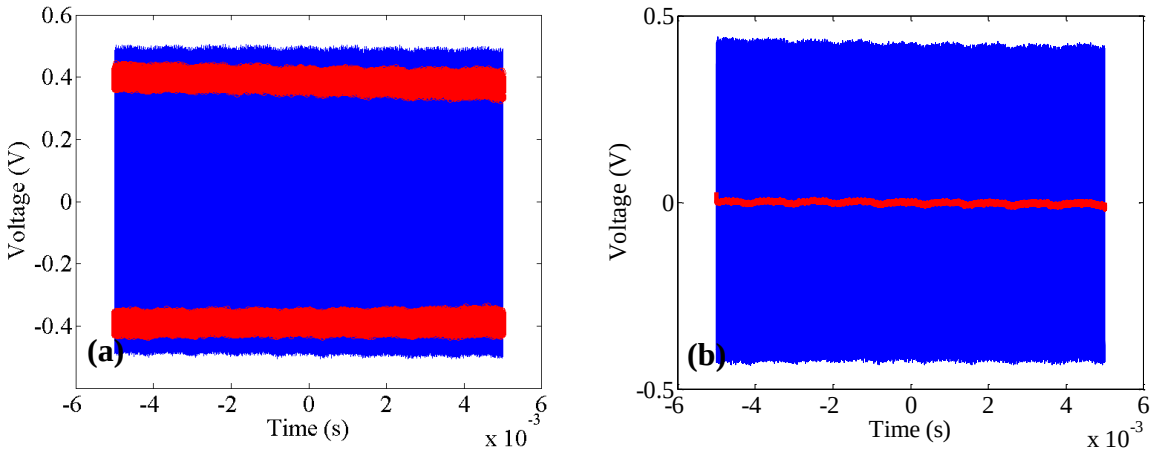

Figure 3.9 – (a) Signal received by the photodetector (blue line). The red circles are the sampling points. (b) down-sampled signal (blue lines). The red line corresponds to the signal point-by-point average.

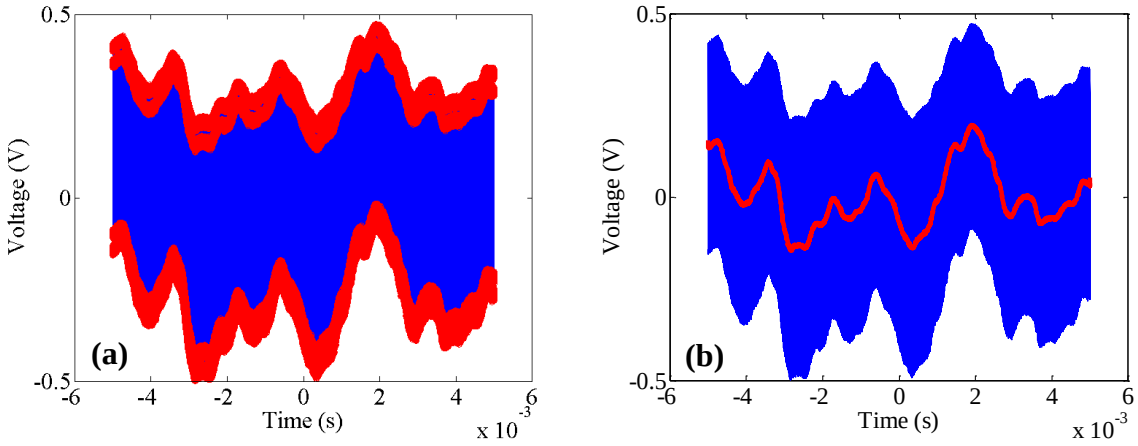

Figure 3.10 – (a) Signal received by the photodetector (blue line). The red circles represent the sampling points. (b) down-sampled signal (blue lines). The red line corresponds to the signal point-by-point average.

When the temperature of the chamber positioned close to the receiver reached 36°C, new data were acquired. The new temperatures were: T1=36°C, T2= 29°C, T3=25°C. In this case, signal fluctuations are evident as visible in Figure 3.10(a). This indicates the presence of a turbulence inside the chamber. Therefore, the signal average (red line Figure 3.10(b)) changes with time, due to the turbulence effects.

Though, the obtained optical turbulence is low (σ_I^2=0.006235) the quality of the link gets worse as shown by the values of the *Q*-factor and the BER: $Q = 3.215$, BER = 6.51×10^{-4}.

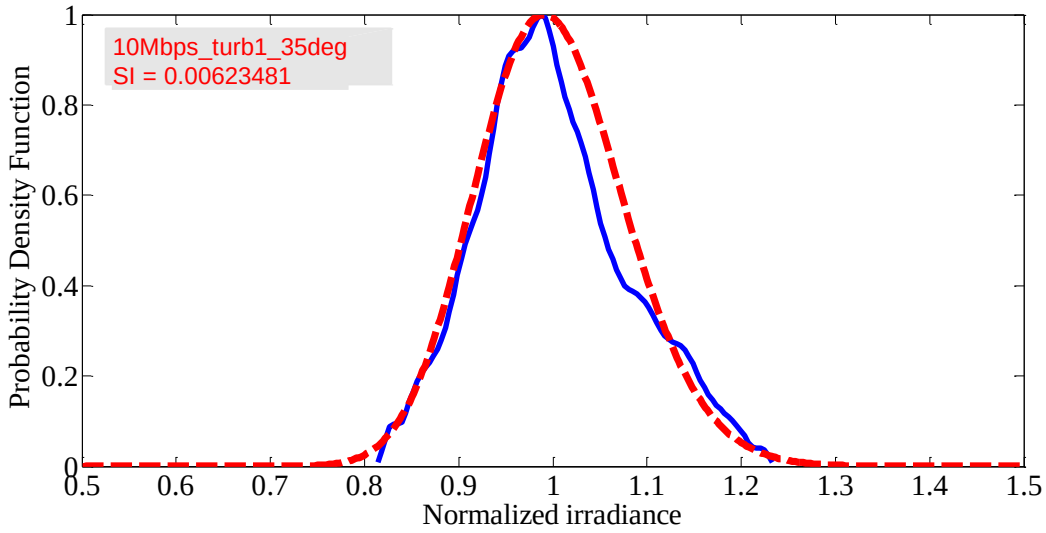

Figure 3.11 – Comparison between the normalized theoretical lognormal distribution (red dashed line) and the normalized histogram of the measured values (blue line) at a Rytov variance of 0.008059 (σ_I^2=0.006235).

Figure 3.11 illustrates a comparison between the normalized lognormal distribution (introduced in Chapter 2) and the normalized histogram of the measured values at a Rytov variance of σ_R^2=0.008059. The latter parameter was derived taking into account the aperture averaging effects. In particular I have used the method explained at the end of Section 1.4.1, and considered a detector size D = 1mm. The comparison shows a good fitting between the theoretical and experimental data. The blue curve is completely inside the theoretical curve, but there is a small discrepancy between them, and this can be due to the small number of samples taken during the acquisition.

Subsequently, the temperature in the compartment increased until it reached the value of 49°C. New data were subsequently acquired. The new temperatures were: T1=49°C, T2= 32°C, T3=26°C.

In this case, the measurement analysis highlights a reduction of the optical turbulence inside the chamber (σ_I^2=0.002589) if compared to the previous case. Consequently, the link performance improved with a greater value of the Q-factor and the BER: Q = 4.9918, BER = 2.99×10^{-7}.

Also in this case, as shown in Figure 3.12, the normalized lognormal distribution and the normalized histogram of the measured values are similar.

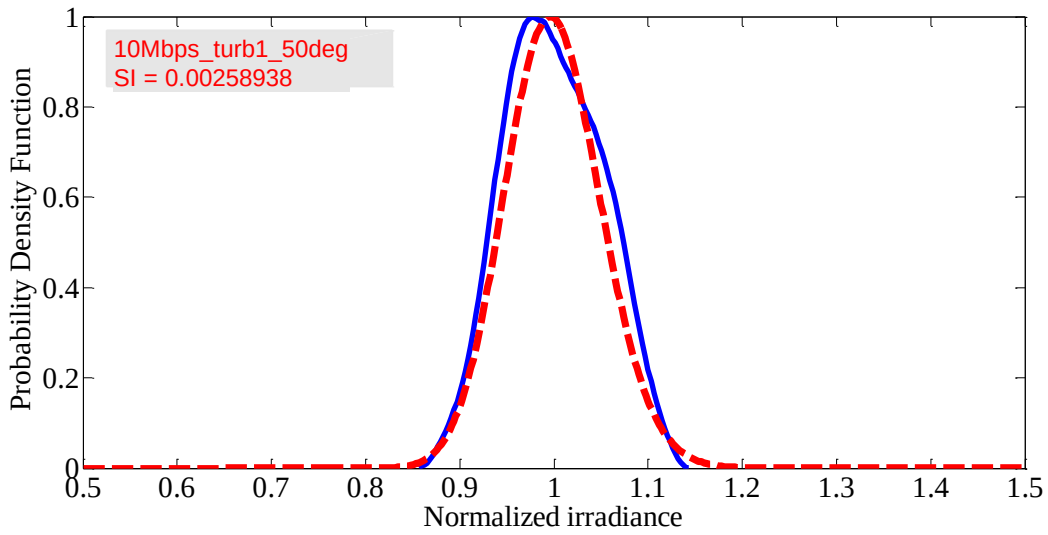

Figure 3.12 – Comparison between the theoretical normalized lognormal distribution (red dashed line) and the normalized histogram of the measured samples at a Rytov variance of 0.003347 (σ_I^2=0.002589).

Experiment 2

Measurement conditions:

- Data rate: 1 Mbps;
- Fan heater close to the transmitter ON: FH1 = OFF; FH2 = OFF; FH3 = ON.

In this case, the measurement taken immediately after turning the heater ON will not be described, as it is not significant and presents no optical turbulence. Instead, a detailed comparison between the two measurements, taken respectively when the temperature reached 35°C and 47°C, will be discussed in the following. In detail, in the first case, the measured temperatures were T1=23°C, T2= 25°C, T3=35°C, while in the second case, they were T1=25°C, T2= 31°C, T3=47°C.

In Figure 3.13, the signal received by the photodetector in both cases (35°C – panel (a) and 47°C – panel (b)) is shown. Signal fluctuations due to the optical turbulence can be seen in both diagrams, and the obtained values of the scintillation index were $\sigma_I^2(35°C)$=0.042807 and $\sigma_I^2(47°C)$=0.055723, respectively. Furthermore, the derived Rytov variance were: $\sigma_R^2(35°C)$=0.055723 and $\sigma_R^2(47°C)$=0.009611. Also in these cases, we can observe a stronger fluctuation at 35°C, rather than at 47°C. The turbulence generated turning ON the heater

positioned close to the transmitter was stronger than that created turning ON the heater positioned close to the receiver.

Figures 3.14 (a) and (b) show the down-sampled filtered signal and the corresponding average (red line) for both cases. Whereas, in Figures 3.15(a) and (b) the PDF of the samples is shown for both cases. As opposite to the previously analyzed cases, the scintillation index obtained was sufficient high, so the Gamma-Gamma model was used to plot the distributions. Also in these cases, a good agreement between the theoretical distribution (red dashed line) and the experimental data (blue dashed line) was observed. A greater value of the samples was responsible of less irregular experimental data less along the lateral sides, thus improving the distribution.

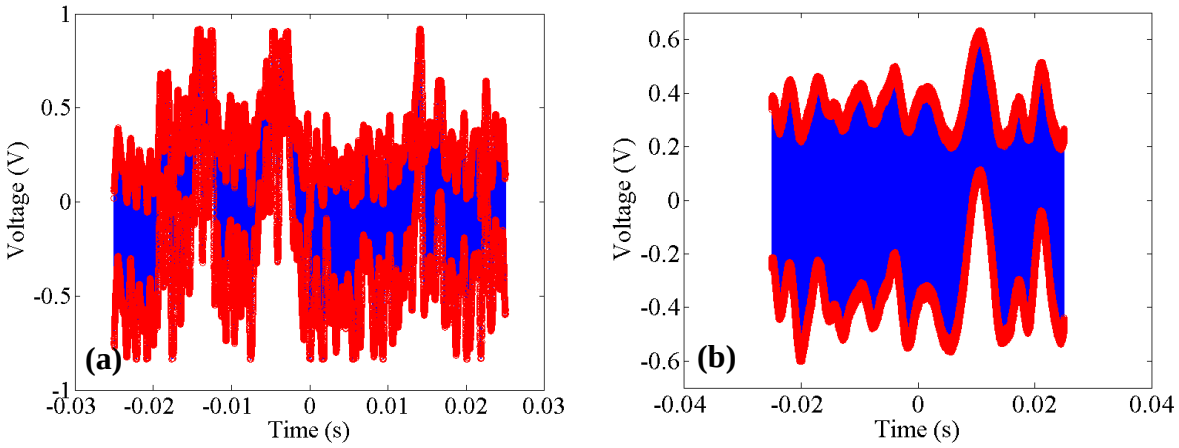

Figure 3.13 – Signal received by the photodetector (blue line) – Rate 1 Mbps: (a) T3 = 35°C; (b) T3 = 47°C. The red circles represent the sampling points.

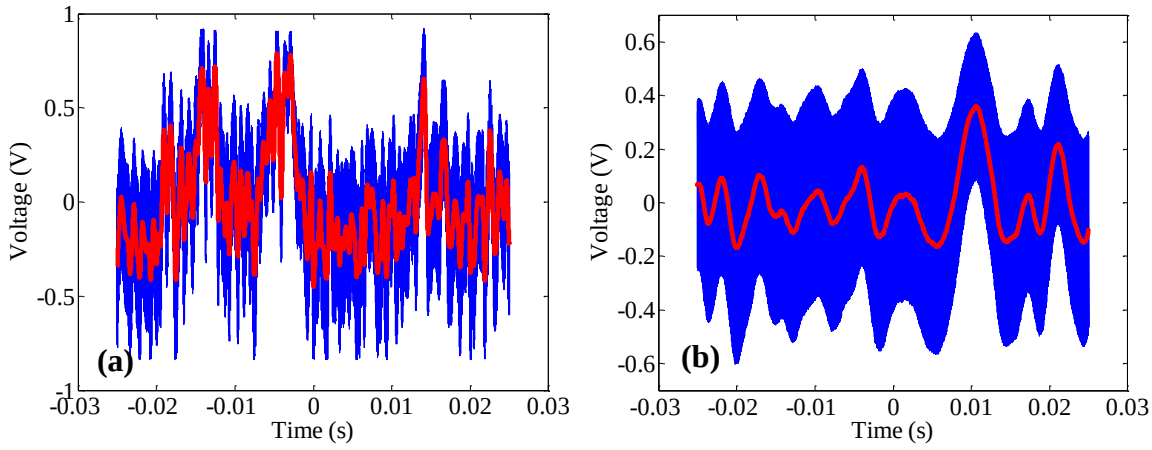

Figure 3.14 – Down-sampled signal (blue lines) - Rate 1 Mbps: (a) T3 = 35°C; (b) T3 = 47°C. The red line corresponds to the signal point-by-point average.

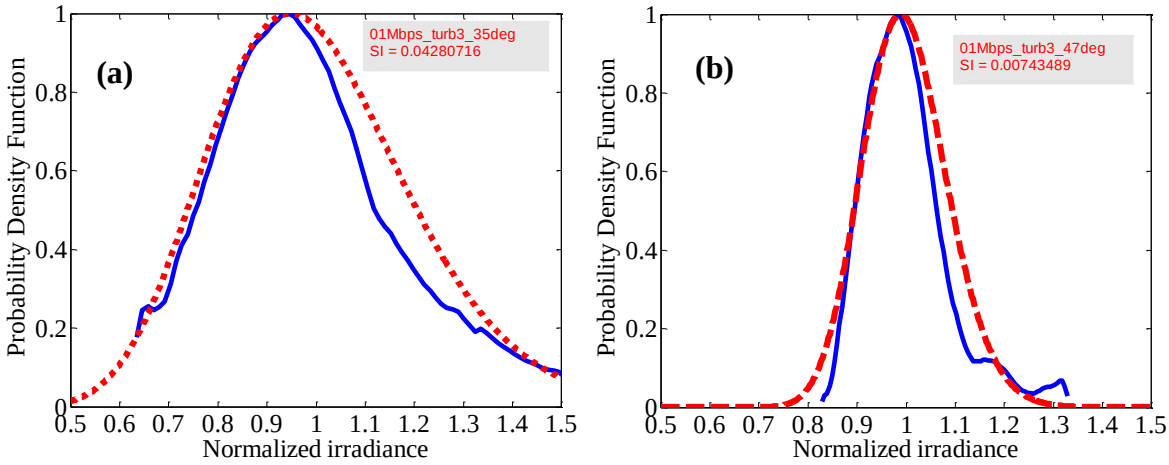

Figure 3.15 – Normalized histograms of the measured samples (blue line) and theoretical normalized Gamma-Gamma distribution (red dashed line) - Rate 1 Mbps:
(a) T3 = 35°C; (b) T3 = 47°C.

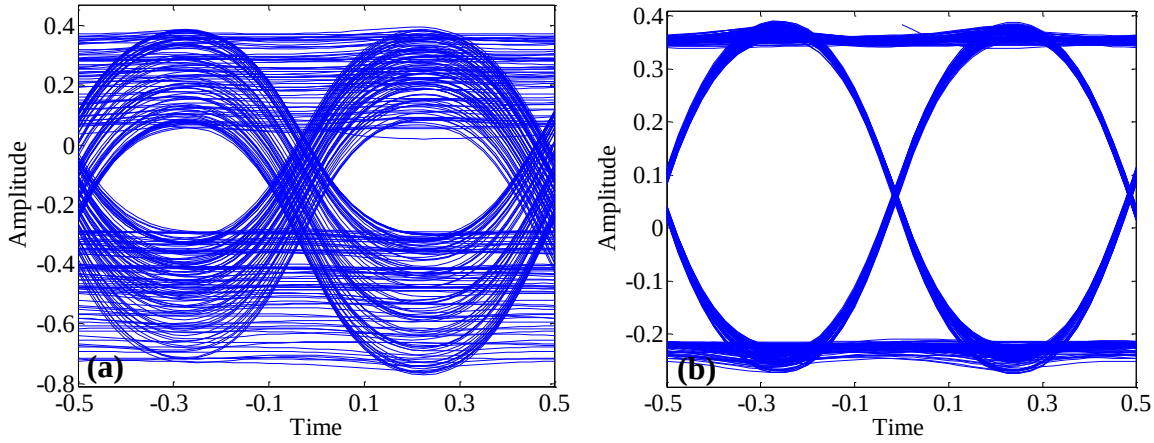

Figure 3.16 – Eye diagram - Rate 1 Mbps: (a) T3 = 35°C; (b) T3 = 47°C.

In Figures 3.16 (a) and (b) the comparison between the two eye-diagrams is shown. In particular, in the case (a) it is very closed because of the presence of a greater strength of the optical turbulence than in the (b) case. In fact, the *Q*-factor and the BER values I have obtained are:

- T3 = 35°C: $Q = 1.8083$, BER = 3.53×10^{-2};
- T3 = 47°C: $Q = 3.1815$, BER = 7.33×10^{-4};

Also these results demonstrate that in the case of T3=35°C, the FSO link quality was worse than in the case of T=47°C.

3.3.3.2 Oven set-up measurements

In this section, the results obtained during the measurements performed using the *oven* set-up, will be described. The results are illustrated in Table 3.6.

As previously described, measurements at varying data rates (1, 5 and 10 Mbps) were performed. For each data rate, when the oven reached the steady temperature (about 160°C), a measurement was taken without turning on the heater (*noturb* case). In this case, no turbulence was created in the oven, and this can be deduced from the low values of the scintillation index (always less than 0.0005).

Later on, for each data rate, the air pump was turned on and the same measurements were performed (*turb* case in the Table 3.6). As it can be seen, the maximum value of the scintillation index was obtained in correspondence of the measurement #2 (at 1 Mbps), getting a value of SI = 0.037729. Therefore, even in this case, it was not possible to obtain greater values of turbulence.

Measure	Q_factor	BER	SI	Rytov variance	SI(0)	Aperture averaging
Case 1 - 1Mbps noturb	18.231	1.46E-74	0.000194	0.00025	0.00025	0.77334
Case 2 - 1Mbps turb	1.6207	5.25E-02	0.037729	0.049042	0.049017	0.76971
Case 3 - 5Mbps noturb	11.3997	2.10E-30	0.000446	0.000577	0.000577	0.77332
Case 4 - 5Mbps turb	1.9472	2.58E-02	0.027385	0.035506	0.035533	0.77069
Case 5 - 10Mbps turb	2.0711	1.92E-02	0.020643	0.026728	0.026763	0.77133
Case 6 - 10Mbps noturb	17.7219	1.42E-70	0.000261	0.000338	0.000338	0.77333

Table 3.6 – Measurements results in the "Oven" set-up.

As mentioned, the measurements with the pump heater turned off (case 1, case 3 and case 6) show low values of the optical turbulence. However, the high temperature inside the oven (around 160°C in each case) generates small visible signal fluctuations, as it can be seen in Figure 3.17. The red circles represent the sampling points chosen to obtain the maximum value of the BER. The FSO link presents good performance at each rate, and at same time shows high values of the *Q*-factor and low values of the BER (see Table 3.6).

Figure 3.18 shows the normalized histograms of the samples for both cases. In these cases, because of the low values of the scintillation index, the log-normal distribution was used to fit the data. A good agreement between the theoretical distribution (red dashed line) and the experimental data (blue dashed line) was found.

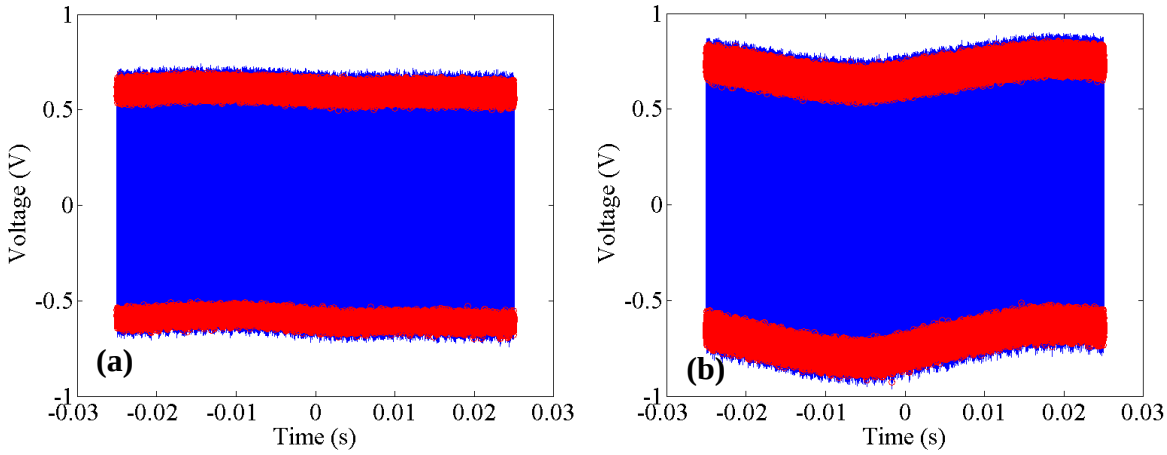

Figure 3.17 – Signal detected by the photodiode (blue line): (a) Case 1 (1 Mbps case), (b) Case 3 (5 Mbps). The red circles represent the sampling points.

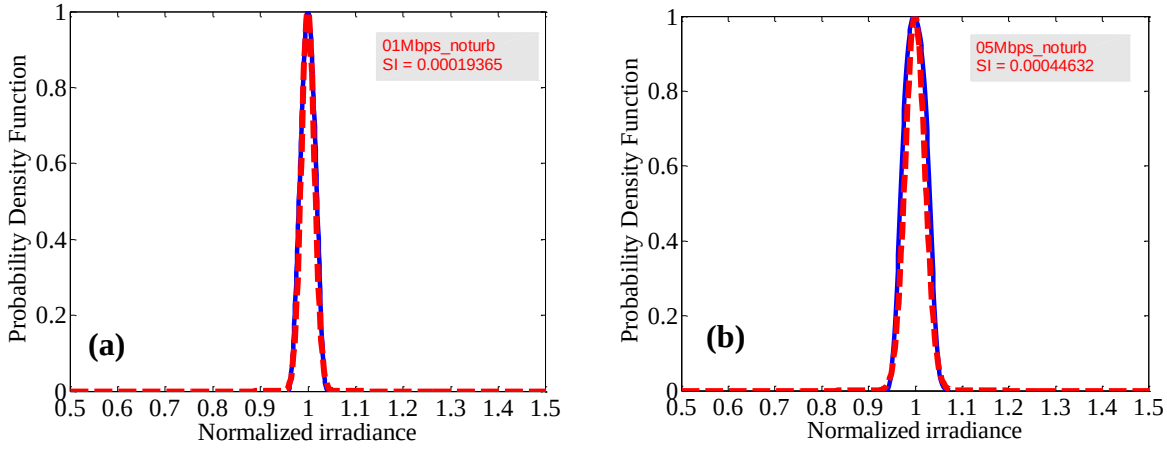

Figure 3.18 – Probability density function (PDF) of the samples (in blue). (a) Case 3 (5 Mbps case), (b) Case 6 (10 Mbps). Red dashed line represents the theoretical log-normal model.

Now, the measurements in which the air pump has been turned on will be described. Also in these cases (Case 2 – 1 Mbps; Case 4 – 5 Mbps; Case 5 – 10 Mbps) the temperature of

the oven was around 160°C. However, the cold air that was pumped inside the oven generated weak turbulence phenomena.

In detail, the measurements taken in Case 2 (1 Mbps) and Case 4 (5 Mbps) will be discussed and compared, whereas the results obtained in Case 5 will not be analyzed, since they do not add anything new to the data discussion. However, the complete results can be found in Table 3.6.

Figures 3.19 (a) and (b) show the signal detected by the photodiode (without the DC component) in both cases. As it can be seen, there are visible fluctuations of the signal that indicate the presence of the turbulence. Figures 3.20 (a) and (b) depict the trend of the down-sampled signal obtained in correspondence of the best *Q*-factor, for both cases.

The red line stands for the signal average value, calculated point-by-point, in correspondence of transition points (level 0 to level 1 and vice versa). Due to the turbulence, there are noticeable fluctuations of the sampled signal and of the signal mean values. The values of scintillation index and of the Rytov variance that I have derived for the case 2 and the case 4 are σ_I^2=0.037729 and σ_R^2= 0.049042; σ_I^2=0.027385 and σ_R^2=0.035506, respectively. These values indicate a weak turbulence.

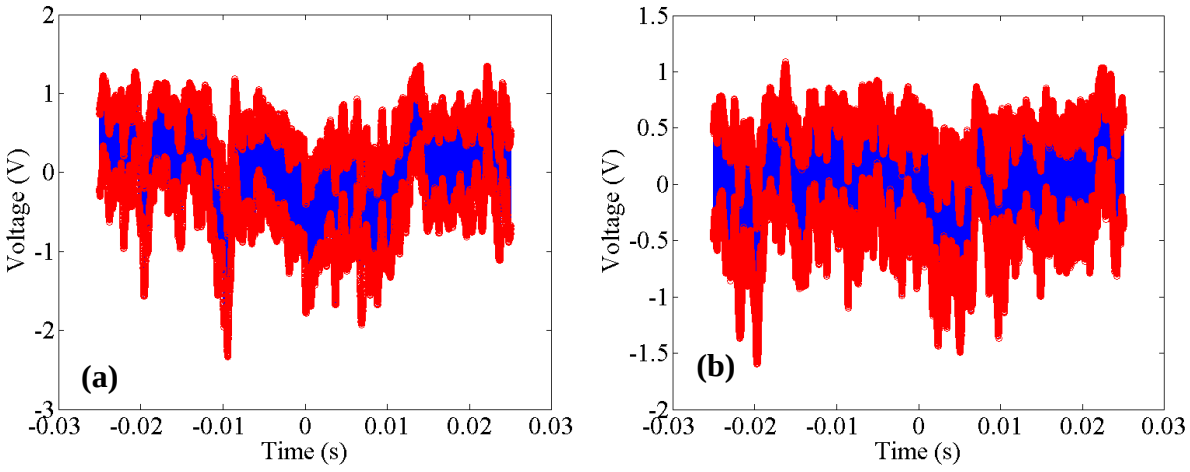

Figure 3.19 – Signal detected by the photodiode (blue line): (a) Case 2 (1 Mbps case), (b) Case 4 (5 Mbps). The red circles represent the sampling points.

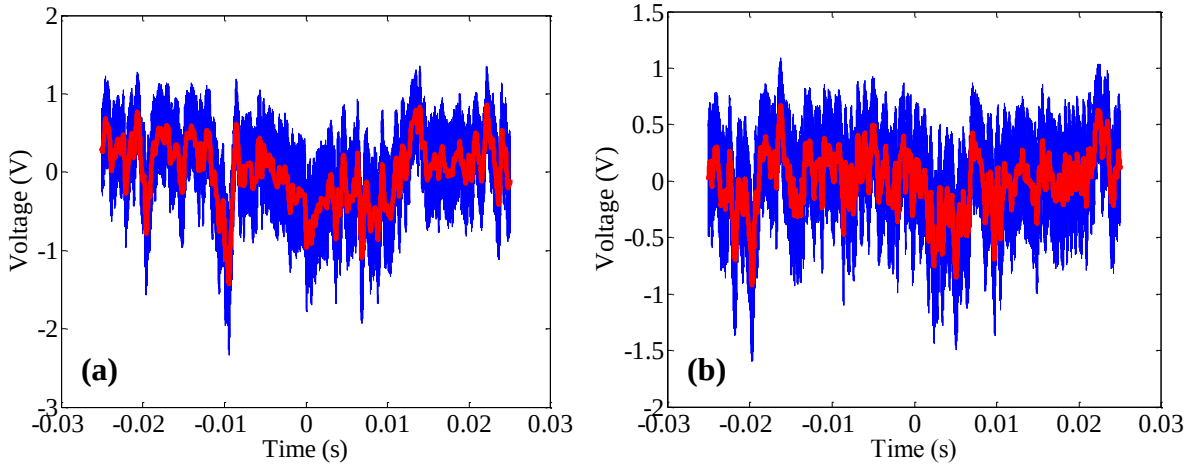

Figure 3.20 – Down-sampled signal (blue lines): (a) Case 2 (1 Mbps), (b) Case 4 (5 Mbps). The red line corresponds to the signal point-by-point average.

In Figures 3.21 (a) and (b) the normalized histograms of the samples are shown for both cases. In this case, the scintillation index obtained is higher than 0.013, so the Gamma-Gamma model was used to plot the distribution. Also in these cases, a good agreement between the theoretical distribution (red dashed line) and the experimental data (blue dashed line) was observed.

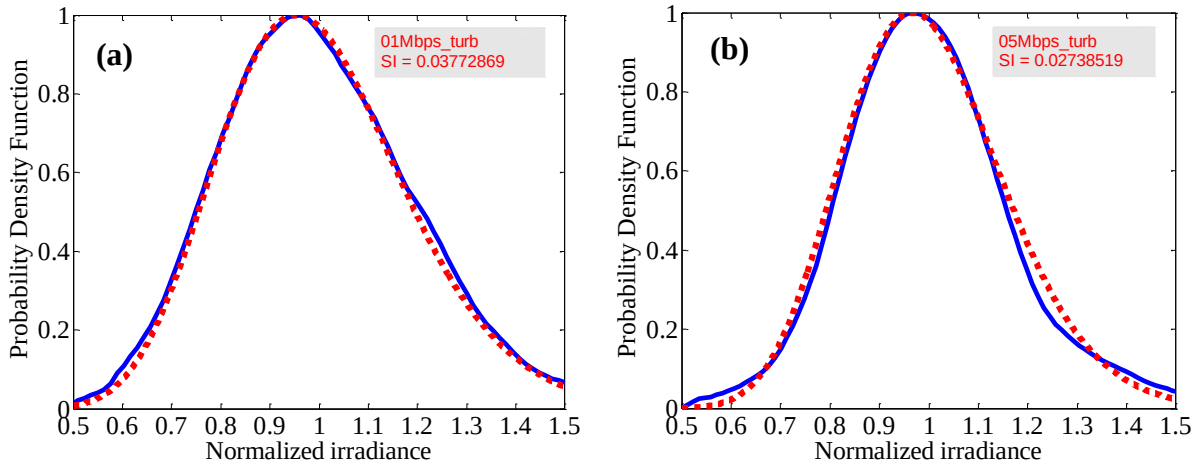

Figure 3.21 – Normalized histograms of the measured samples (blue line) and theoretical normalized Gamma-Gamma distribution (red dashed line):
(a) Case 2 (1 Mbps); (b) Case 4 (5 Mbps).

3.3.3.3 Scintillation index evaluation using C_T^2

Another approach to calculate the optical turbulence strength in a FSO link is the evaluation of the temperature structure constant C_T^2. In this section, I will present the results that I have obtained, applying this method, to the measurement results collected using the indoor atmospheric chamber.

Considering a plane wave propagation and a zero inner scale for the expression (3) of the Chapter 1, we can have [1,2]:

$$\langle (T_1 - T_2)^2 \rangle = C_T^2 \, R^{2/3} \tag{2}$$

where T_1 and T_2 denote the temperature at two points separated by the distance R (in meters). Under this hypotheses, the refractive index structure parameter C_n^2 can be calculated using the following expression:

$$C_n^2 = \left(79 \times 10^{-6} \frac{P}{T^2}\right)^2 C_T^2 \tag{3}$$

where P is the atmospheric pressure in mbar, T is the temperature expressed in Kelvin.
As previously described, from the C_n^2 we can obtain the values of the Rytov variance by the formula:

$$\sigma_R^2 = 1.23 C_n^2 k^{7/6} R^{11/6} \tag{4}$$

where k is the wavenumber, R [m] is the distance between two adjacent thermometers.

The temperatures, collected during the measurements in the indoor chamber, permitted me to evaluate the thermal gradient in each examined area and thus to compute the C_T^2 from the expression (2). I have also derived the C_n^2 by the expression (4) considering an atmospheric pressure P = 1013.25mbar and a room temperature T = 297.15K. Finally, I could calculate the values of the Rytov variance by the equation (3). The scintillation index was directly derived by the Rytov variance using the expression (10) presented in Chapter 1.

Table 3.7 shows the details of the temperature measurements and the values of the scintillation indices calculated using the two above mentioned different methods.

As it can be seen, there is an order of magnitude of difference between them. However, the values obtained for the refractive index structure parameter are similar to those reported in [2] using the same measurement set-up.

In Figure 3.22 the comparison between the theoretical scintillation index calculated starting from C_n^2 values and the scintillation index acquired during the measurements campaign is shown. As it can be seen, in the case 5 Mbps *turb3* cases (fan heater positioned close to the transmitter ON, and the other two OFF), there is a good agreement between the theoretical trend and the measured results. Instead, in the case (b) 10 Mbps *turb1* cases (fan heater positioned close to the receiver ON, and the other two OFF) the good agreement occurs only at 28°C and 36°C, while there is almost an order of magnitude of difference at 49°C. The reason of this behavior has already been previously described.

Measure	T1	T2	T3	Cn^2	SI(D) C_T^2 approach	SI(D) measured
OOK_01Mbps_turb1_25deg	25	28	26	8.88E-13	0.00079743	0.000028
OOK_01Mbps_turb1_50deg	50	33	26	2.31E-11	0.020751	0.004279
OOK_01Mbps_turb3_35deg	23	25	35	7.10E-12	0.0063856	0.042807
OOK_01Mbps_turb3_47deg	25	31	47	1.99E-11	0.01793	0.007435
OOK_05Mbps_turb1_29deg	29	27	25	5.46E-13	0.00049068	0.000025
OOK_05Mbps_turb1_33deg	33	28	25	2.32E-12	0.0020863	0.000964
OOK_05Mbps_turb1_46deg	46	33	28	1.32E-11	0.011914	0.001171
OOK_05Mbps_turb3_26deg	24	26	26	2.73E-13	0.00024532	0.000070
OOK_05Mbps_turb3_35deg	24	28	35	4.44E-12	0.0039899	0.005872
OOK_05Mbps_turb3_50deg	26	32	50	2.46E-11	0.022099	0.009998
OOK_10Mbps_turb1_28deg	28	27	25	3.41E-13	0.00030665	0.000138
OOK_10Mbps_turb1_36deg	36	29	25	4.44E-12	0.0039899	0.006235
OOK_10Mbps_turb1_49deg	49	32	26	2.22E-11	0.019954	0.002589
OOK_10Mbps_turb3_25deg	25	26	25	1.37E-13	0.00012265	0.000139
OOK_10Mbps_turb3_33deg	25	28	33	2.32E-12	0.0020863	0.072830
OOK_10Mbps_turb3_47deg	28	36	47	1.26E-11	0.011362	0.015774

Table 3.7 – "Chamber" set-up - C_n^2 theoretical calculation results and comparison between the scintillation index calculated using C_n^2 and that one calculated by data acquired during the measurements campaign

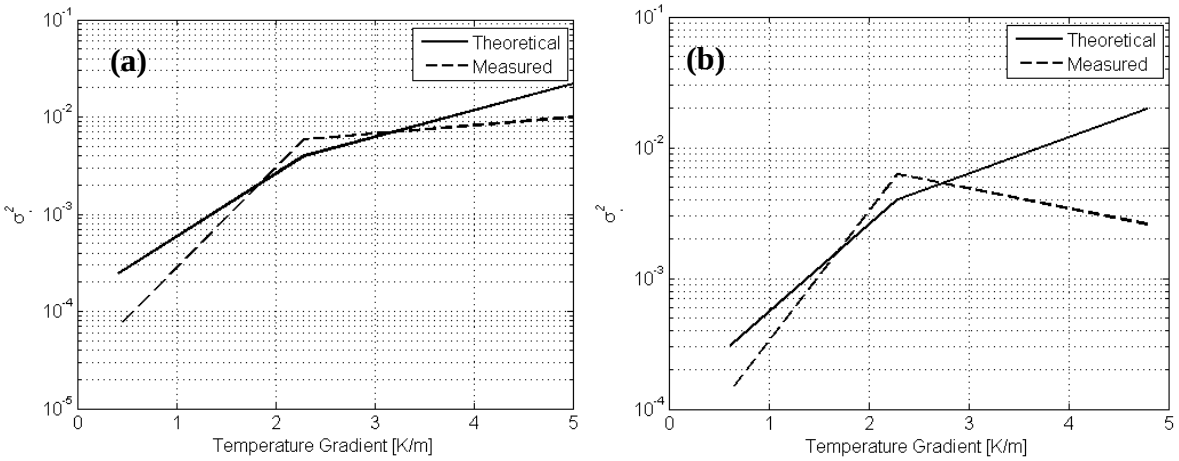

Figure 3.22 – Theoretical scintillation index (solid line) calculated starting from Cn^2 values compared to the scintillation index acquired during the measurements campaign (dashed line). (a) 5 Mbps (*turb3* cases); (b) 10 Mbps (*turb1* cases).

References

[1] L. C. Andrews, R. L. Phillips, and C. Y. Hopen, "Laser Beam Propagation through Random Media," SPIE Press, Bellingham, WA, 2nd edition, 2005.

[2] L. C. Andrews, R. L. Phillips, and C. Y. Hopen, "Laser Beam Scintillation with Applications," SPIE Press, Bellingham, WA, 2001.

[3] Z. Ghassemlooy, H. Le Minh, S. Rajbhandari, J. Perez, and M. Ijaz, "Performance Analysis of Ethernet/Fast-Ethernet Free Space Optical Communications in a Controlled Weak Turbulence Condition," Journal of Lightwave Technology, vol.30, no.13, pp. 2188-2194, 2012.

[4] W.O. Papoola, Z. Ghassemlooy, C.G. Lee and A.C. Boucouvalas, "Scintillation effect on intensity modulated laser communication systems a laboratory demonstration," Optics and Laser technologies, Elsevier, 2010.

[5] S. Zvanovec, J. Perez, Z. Ghassemlooy, S. Rajbhandari, and J. Libich, "Route diversity analyses for free-space optical wireless links within turbulent scenarios," Optics Express, Vol. 21, Issue 6, pp. 7641-7650, 2013.

Chapter 4

"Rateless codes for error mitigation in FSO links"

4.1 Introduction

As previously introduced, FSO communications offer several advantageous features but they, unfortunately, suffer from several impairments that limit their performance: absorption, scattering and optical turbulence. Channel models and measurement campaigns were introduced in the previous chapters. They highlight the optical turbulence degradation of the communication performance and, moreover, introduce depth fadings. The burst errors caused by the latter are responsible for a big data losses, and, in particular, occurred at high data rate transmission.

In order to improve FSO communications afflicted by the optical turbulence, I have proposed to employ a new typology of transmission codes, suitable for erasure channels: rateless codes. Adding repair symbols to source symbols, they are able to recover all the source data with high probability despite burst errors. Moreover, they can manage large amounts of data and do not need retransmission. I have investigated on the rateless codes performance in FSO links by a simulation campaign. In detail, I have analyzed three different rateless codes in two different FSO link typologies by using the previously introduced channel models, to predict irradiance fluctuation due to optical turbulence. The results of simulations, that take into account the rateless codes, will be discussed in the following.

This research work was supported by the European Space Agency under the grant no. 5401001020.

4.2 Rateless codes

Rateless codes are named “rateless” as the rate of these code typologies is not fixed *a priori*. Therefore, they are able to adapt themselves to the channel conditions in order to reduce the errors that occur during a communication. This is an important feature for the rateless codes but the most relevant novelty they have introduced is their capability to recover all the source data, with high probability and without any errors, using protocols that do not employ any retransmission procedures. The above-mentioned features are suitable for fading channels, that present erasure errors, for multicast/broadcast communications and for each communication channel that needs adaptive codes.

In order to well describe the functionalities of rateless codes, I will present the Fountain codes: the first codes of the rateless category. I will also present three rateless code typologies, that are more used in literature and in experimental applications: Luby Transform, Raptor and RaptorQ.

4.2.1 Fountain codes

Fountain codes (FCs) [1] are rateless and are the first rateless codes that have been developed. They do not need feedback: in fact, they add to the source data a redundant coding (also settable on the fly) that allows the receiver to recover the whole payload, despite erasure errors. More in detail, random linear FCs produce, starting from a group of K symbols, a new set of N encoded symbols (with $N > K$) that theoretically could be infinite. Each generated encoded symbol will be linked to one or more source symbols (the number of such links is termed “degree” (δ)) according to a specific distribution. In particular, the encoded symbols have been obtained by a linear combination (bitwise sum, modulo-2) of the K source symbols by means of a binary pseudo-random generator **G** matrix ($K \times N$). The **G** matrix depends on the degrees distribution and, for this reason, its definition is crucial for the code implementation. The receiver that detects a $K+\varepsilon$ number of encoded symbols (where ε is the received overhead) is able to recover the source data with a probability that increases with an ε increase.

Therefore, the encoder represents the fountain, the encoded symbols are the droplets and the receiver is the glass. When a number of droplets slightly greater than K is collected in

the glass the decoding process can be done. At this point, if more droplets are collected in the glass there will be more chances that the decoding will be successful.

The details of the Fountain codes encoding/decoding procedures will be described in the following. The encoder steps to produce a symbol t_n (encoding process) are:

1. The source file is divided in *K* symbols with a specific size, named s_1, s_2, s_3,…;
2. *K* random bits are generated for each group of *K* source symbols to build a new column of a binary generator **G** matrix. The latter has a *K* number of rows and an indefinite number of columns;
3. The nth encoded symbol is obtained by a linear combination (bitwise sum, modulo-2) between the *K* source symbols and the nth column of the **G** matrix:

$$t_n = \sum_1^N s_k G_{kn} \tag{1}$$

where s_k is the kth source symbol and G_{kn} is the entry of **G** in row *k* and column *n*.

During communications, several errors could occur, causing symbol losses. Figure 4.1 shows an example of a generator **G** and the received matrices. In particular, the grey columns in Figure 4.1 are related to the lost symbols. Supposing that the receiver collects *N* encoded symbols and that is able to rebuild the G matrix ($K \times N$), three cases can be considered:

1. $N<K$: in this case, the recovery is not possible;
2. $N=K$: it is possible to recover the source symbols if and only if the received **G** ($K \times K$) matrix has a maximum rank of *K*. In fact, in this case, **G** is invertible and the source symbols s_k can be derived by means of the following expression:

$$s_k = \sum_1^N t_n G_{nk}^{-1} \tag{2}$$

3. $N>K$: as the previous case, the recovery is possible if **G** ($K \times N$) has a maximum rank of *K*. Of course, in this case, it is more probable that the recovery condition is satisfied.

Several classes of rateless codes were developed in literature. In the following, I will present the most important and efficient ones: Luby Transform, Raptor and RaptorQ codes.

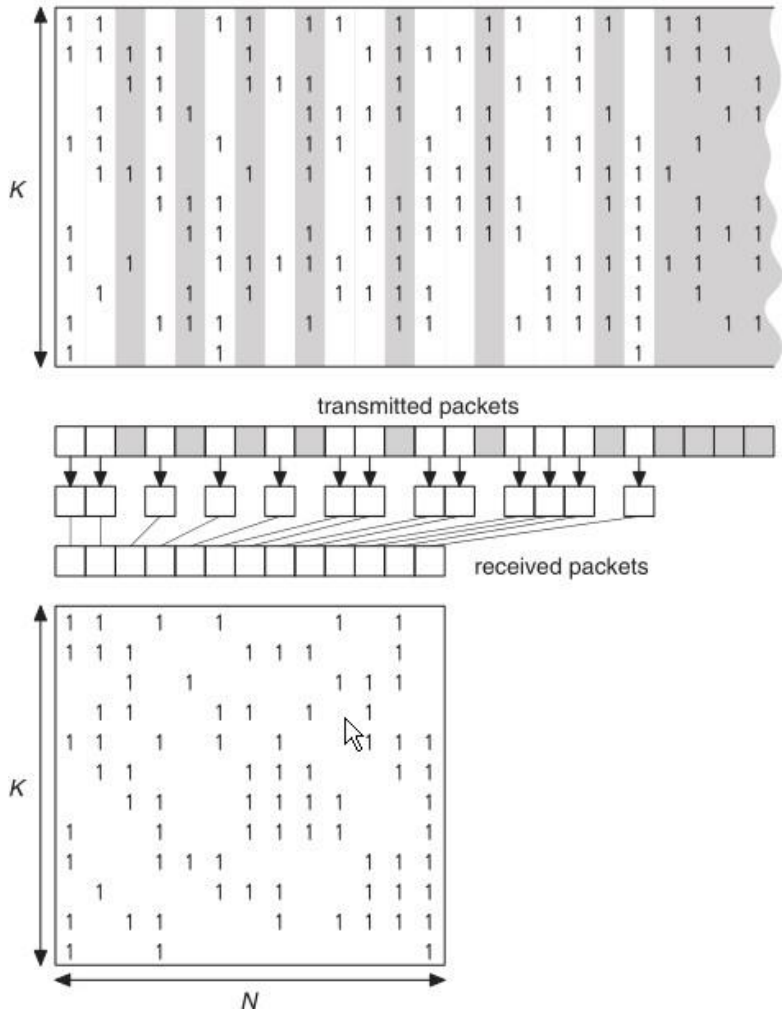

Figure 4.1 – Generator **G** matrix (above) and received **G** matrix (below) [1]

4.2.2 Luby Transform codes

The Luby Transform (LT) codes [1,2] were introduced by Michael Luby and they are a rateless code typology. For the encoding process, they use a degree distribution to define the number of the source symbols that are employed to generate each encoded symbol. In detail, the encoding steps are the following:

1. Random selection of the degree d_n according to the employed degree distribution;
2. Random selection of d_n source symbols;
3. Bitwise sum (modulo-2) of the selected source symbols.

The encoding process can be illustrated by means of a graph. An example of LT encoding diagram is depicted in Figure 4.2. The grey circles are the source symbols, the green circles are the encoded symbols and the edges are the links between source and encoded symbols. The number of edges related to an encoded symbol is the degree. If the average degree is low, the graph will be sparse.

The purpose of the decoding procedure is to recover the source symbol s_k from the encoded symbols t_n using the relation $\boldsymbol{t}=\boldsymbol{sG}$, where $\boldsymbol{t}$ and $\boldsymbol{s}$ are vectors and $\boldsymbol{G}$ is the generator matrix. In order to solve this problem, LT codes employ the *message passing* [1,3]. The LT decoding algorithm is the following (the encoded symbols t_n are the check nodes):

1. Find the check nodes with only an edge (degree equal to 1). If there are no check nodes, with this characteristic, the decoding fails;
2. Set $s_k = t_n$;
3. Add s_k to all the other check nodes connected to s_k;
4. Remove all the edges connected to s_k;
5. Repeat the iteration until all source symbols are obtained;

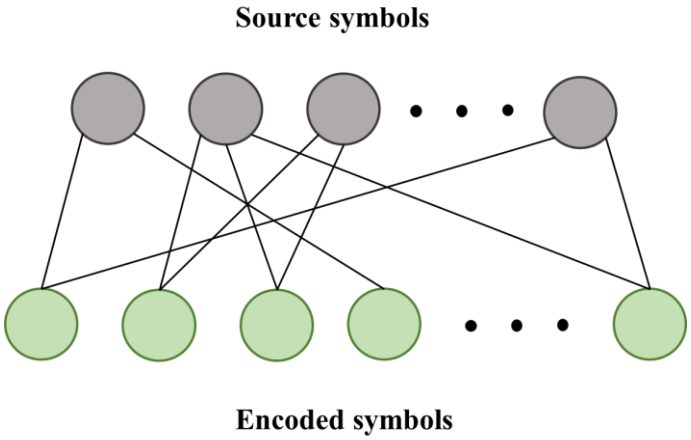

Figure 4.2 – Example of an encoding graph

Figure 4.3 shows an example of decoding steps in the case of binary symbols. The graph is composed of three source symbols (s_1,s_2 and s_3) and four received symbols (t_1=1,t_2=0,t_3=1, t_4=1). Each box illustrates the above mentioned decoding procedure. The last box f) depicts the recovered source symbols.

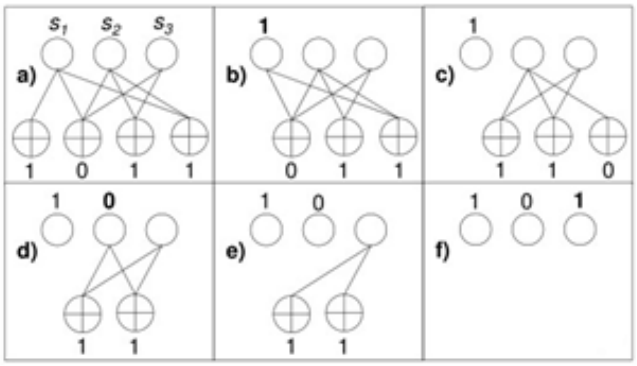

Figure 4.3 – LT decoding example with *K*=3 source bits and *N*=4 encoded bits [1,3]

The degree distribution has an important role in LT codes. It has to satisfy three important points: the encoded symbols have to permit to recover all the source symbols; at each iteration, we have to find at least a check node with a single edge; the number of recovery symbols should be as small as possible. Ideal Soliton Distribution offers these features and it has been defined by the following expression:

$$\begin{cases} \rho(1) = 1/K \\ \rho(d) = \frac{1}{d(d-1)} \end{cases} \qquad d = 2,3,\dots,K \tag{3}$$

Unfortunately, this distribution is poorly in practice, because fluctuations around the expected behaviour make it very likely that at some point, in the decoding process, there will be no degree-one check nodes [3]. The robust soliton distribution overcomes these problems and is defined as follows:

$$\mu(d) = [p(d) + \tau(d)]/Z \tag{4}$$

where

$$Z = \sum_d p(d) + \tau(d) \tag{5}$$

$$\tau(d) = \begin{cases} \frac{S}{K}\frac{1}{d} & d = 1,2,\dots,(K/S) - 1 \\ \frac{S}{K}\log(S/\delta) & d = K/S \\ 0 & d > K/S \end{cases} \tag{6}$$

δ is a bound that causes the failure of the decoding process when *K'* encoded symbol are received, *S* is a parameter that is given by:

$$S = c \ln(K/\delta)\sqrt{K} \tag{7}$$

where *c* is an arbitrary constant usually less than 1.

Figure 4.4 illustrates the $\rho(d)$ and $\tau(d)$ distributions for K=10000, c=0.2 and δ=0.05. The small-d end of τ ensures that the decoding process starts. Moreover, the spike in τ at d=K/S ensures, with good probability, that each source symbol is linked at least one check node [1,2]. The decoding and encoding complexity of LT codes scales as $\log_e(K)$ per packet, because the average degree of the packets, in the sparse graph, is $\log_e(K)$. Therefore, LT codes have a total complexity of $K \cdot \log_e(K)$. Nevertheless, the used degrees distribution does not always guarantee a decoding sparse graph and, consequently, the best decoding speed [1]. Raptor codes [4,5], introduced by Shokrollahi in 2003, overcome this issue as they have a complexity linearly dependent on *K*.

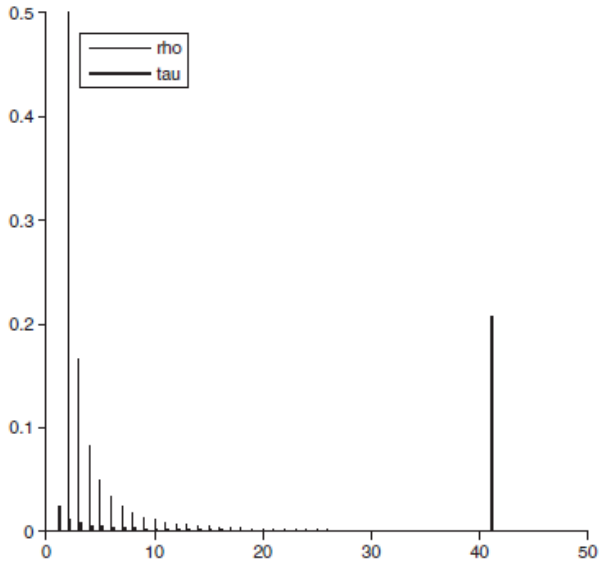

Figure 4.4 – $\rho(d)$ and $\tau(d)$ distributions for K =10000, c=0.2 and δ=0.05 [1,3]

4.2.3 Raptor and RaptorQ codes

The LT codes lower bound of $K \cdot \log_e(K)$ is due to the fact that each source node of the decoding graph has to be connected to, at least, an edge. In Raptor codes (RCs) a fraction of the source node can have no connections with any edge. Nevertheless, in order to have this feature, Raptor codes employ Forward Error Correction codes to recover the missing connection. However, the LT codes remain the most important part of the whole code.

Figure 4.5 depicts a schematic diagram of Raptor codes where K=16 source symbols are encoded in L=20 pre-encoded symbols by means of an outer code. In turn, the latter symbols are encoded in N=18 output symbols by a weakened LT code. The average degree of the output symbols is equal to three. The weakened LT code connects just 17 pre-encoded symbols to the output symbols, whereas the remaining 3 symbols (highlighted in grey) do not have any connection. In the decoding process the weakened LT codes will recover the 17 pre-encoded packet and, finally, the outer-code will recover the 16 source symbols. The encoding/decoding complexity scales linearly with the file size [1].

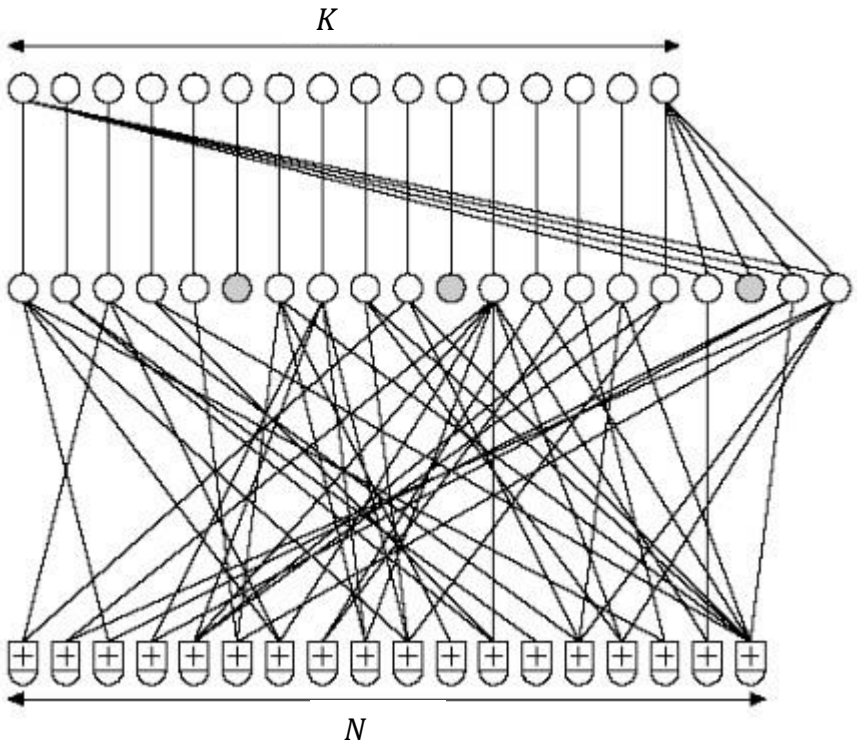

Figure 4.5 – Schematic diagram of Raptor code [1]

Raptor codes can use different outer codes classes (Shokrollahi employs an irregular Low Density Parity Check) and degree distribution for LT codes. Moreover they can be non-systematic or systematic. In the latter case, the first *K* encoding packets are the same as the *K* source packets and the last *N-K* repair symbols are the result of encoding [6]. For the performance study, systematic Raptor codes (implemented as described in the RFC 5053) were used [5]. They work on the Galois Field 2 (GF(2)) and can offer a maximum number of source symbols equal to 8192 [7].

RaptorQ (RQ) codes are an evolution of RCs [8]. They are also systematic codes but they work on a much larger alphabet, in particular on GF(256). It can be demonstrated that with a larger alphabet, the failure probability is reduced at a certain overhead [9]. Nevertheless, large alphabets require a greater complexity. Shokrollahi and Luby have designed RaptorQ using an efficient outer code defined in the field GF(256) for pre-coding step. Furthermore, the other encoding/decoding steps have been improved if compared to the Raptor codes. In this way, they obtained a good trade off between performance and recover capabilities [7].

Raptor codes can manage a maximum number of symbols equal to 8192 since, when *K* exceeds this value, the failure probability at null overhead is about 1. In these cases, it is difficult to find good systematic indices to execute the encoding/decoding process [7].

Instead, better overhead/probability-of-failure performance of RaptorQ codes, if compared to Raptor codes, permit to easily find systematic indices, also at high values of *K* [7]. Hence, RaptorQ supports a number of source symbols much larger than Raptor.

For the following analyses of the recovery capabilities performance, I have used RaptorQ codes implemented considering the RFC 6063 developed by Shokrollahi, Luby and Watson [8].

4.3 Simulator architecture

In FSO communications, at the receiver, the irradiance fluctuations cause communication failures and outages, when irradiance values drop below a fading depth (threshold under which the receiver is not able to detect any data). In other words, when the optical signal drops below the above mentioned fading depth threshold, we can interpret it as an erasure error occurring in the FSO communication link.

It is also worth noting that at relatively strong turbulence conditions, power fluctuations become larger and, hence, the average value of the signal power decreases. For these reasons, in this work, I have referred to the normalized average value of the signal power and, in particular, to the normalized average value of the irradiance at the receiver.

Using the channel model described in the previous section, we have investigated the outage statistics and the performance of rateless codes at a fast data rate. In detail, we have tested the LT codes and RCs capabilities in order to mitigate erasure errors, which can be detected in a 500 m terrestrial free space link. In our simulations, we have used a 1550 nm wavelength.

In addition, we have not considered the noise due to the photodetector, because it can be neglected if compared to the irradiance fluctuations caused by the scintillation phenomena in the turbulence conditions taken into account. In detail, we have considered the photodetector Noise Equivalent Power (NEP) (i.e., the minimum detectable input power), of 6dB and 9dB lower than the mean value of the irradiance at the receiver. Consequently, the latter is not constant, but varies with the turbulence conditions [10].

For the simulations considered in this section, I have employed an architecture that is described by the block scheme depicted in Figure 4.6. In order to carry out the simulation, I have considered that the encoded symbols represent the output symbols generated by LT codes, Raptor, or RaptorQ codes. In order to carry out the simulation, it is not important to know which data they contain but, rather, how many encoded symbols will be lost during the communications. For this reason, the block "encoded symbols" gives the information about the encoding process. In particular, it contains the number of source symbols K and also the overhead size in percentage (O). This operation is necessary in order to derive the number of the repair symbols $K_r = K \times O$.

For example, if we set K=1000 and an overhead of 20%, we have a $Kr = K \times 0.2 = 200$ and, thus, we have to consider a whole number of encoded symbols equal to $K+Kr$=1200. In order to well describe the recovery capabilities of the three different rateless codes in the simulations, I have used several values of K and overhead.

The transmission block defines the value of the sampling frequency, that will be employed by the irradiance time-series generator, according to the given transmission rate R and the symbol size T.

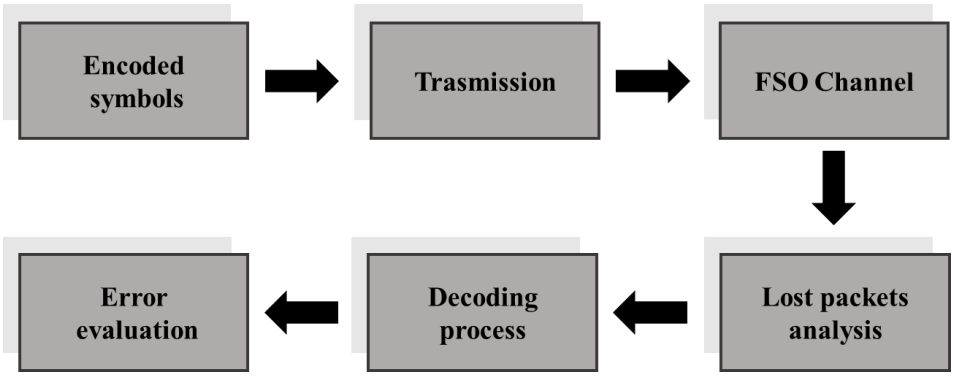

Figure 4.6 – Block scheme of the simulator architecture

Irradiance fluctuations are slow if compared to the data transmission, thus we have considered that a group of data symbols owns the same irradiance value. In order to have a good temporal resolution, I have chosen a time spacing ($t_s=1/f_s$) with the following specifications:

- the value of t_s is around 10μs;
- the value of t_s is proportional to the symbol time t_{sym} with a factor n.

Therefore, the time spacing is given by:

$$t_s = nt_{sym} \tag{8}$$

where n is the number of symbols such that $nt_{sym}\approx 10$, and the symbol size is given by the following expression:

$$t_{sym} = \frac{T}{R} \tag{9}$$

Finally, the sampling frequency can be derived from the following:

$$fs = \frac{1}{t_s} t_s = \frac{1}{nt_{sym}} \tag{10}$$

The FSO channel model, that was implemented for the simulation, works as a Packet Erasure Channel, i.e., a communication channel model where sequential packets are either received or lost [11]. In particular, the "FSO channel block" adds irradiance fluctuations, due to the optical turbulence, to the transmission. This task is carried out by the channel models described in Chapter 2. The optical turbulence strength is defined by the Rytov variance that is

a parameter introduced in Chapter 2: the larger is the value, the higher is the optical turbulence.

As mentioned, due to the optical turbulence several fadings can occur during communications causing erasure errors. In these cases some symbols are lost and the receiver has to carry out a decoding process to recover the source data. The "lost packets analysis" block sets a fading depth as a threshold (under which the receiver is not able to detect data) and, so, determines how many and which symbols get lost. This information is important for the decoding step. In fact, if the received symbols are less than *K*, the decoding process cannot start and, hence, all the source symbols cannot be decoded. Otherwise, the decoding process can start and the probability that the recovery succeed increases with the received overhead.

For the error evaluation, the simulator simply performs the ratio between the decoding failures and the total block size (*K*+*Kr* symbols). This ratio corresponds to a packet loss since, a not recovered block corresponds to *K* source lost symbols.

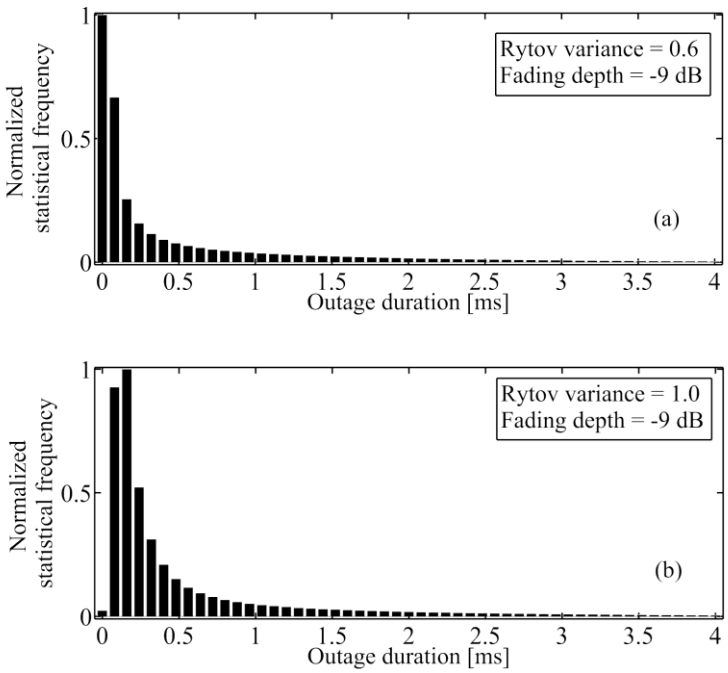

Figure 4.7 – Outage statistics histogram for a -9dB fading depth at a Rytov variance: (a) 0.6; (b) 1.0 [10].

4.4 Simulation results

4.4.1 Outage statistics

In Figure 4.7 outage statistics histograms are depicted. They correspond to a simulation of a ten hours FSO communication link at two different values of σ_R^2 and with a -9 dB fading depth. We can actually see that as σ_R^2 increases, the average outage grows. At different fading depths, I have found a similar behaviour. Therefore, I wondered if I were able to reduce or to eliminate communications errors by using rateless codes and, if so, what configuration parameters should be set. In order to answer these questions, I have chosen to employ modern code typologies belonging to the rateless codes family. In particular, I have used LT codes, RCs and RQ codes [10].

4.4.2 Terrestrial FSO link

I have tested the performance of LT codes and RCs by simulating an OOK modulated transmission at 100 Mbps (1518 bytes frame size) over a distance of 500 m, at different fading depths and σ_R^2 values. More in detail, for each couple of the latter parameters, I have evaluated the failure probabilities (for 1000 points) for an overhead ranging from 5% to 50% and for different values of *K*. Figure 4.8 shows the results concerning to the case of -6dB fading depth and σ_R^2 = 1.0. As expected, when the overhead becomes larger, the decoding performance of both codes improves. Nevertheless, while LT codes are not always able to recover all the source data (i.e., the failure probability is always above 10^{-2}), RCs are able to recover all the source data starting from *K*=500 and for a 50% overhead. Therefore, using the above-mentioned configurations, I was able to demonstrate that the RC failure probability can reach values below 10^{-3}. However, the best performance is given for *K*=1000 and starting from a 35% overhead. Figure 4.9 shows the failure probability versus source packets number, for LT codes and RCs, at different overhead values. I have highlighted that the performance of LT codes increases with *K*, more than the RCs one. This is due to the fact that the performance of RCs is already good, even at low *K* values. I carried out further tests in order to evaluate the performance of the RQ codes. The same configurations I have used for LT codes and RCs have been exploited herein. The failure probability versus overhead percentage related to RQ codes is depicted in Figure 4.10.

We can see how RQ codes are able to recover all the source data starting from K=500 and for a 35% overhead. For higher values of K the performance improves, so that an overhead less or equal to 25% is sufficient enough to recover data for K > 2000 [10,12].

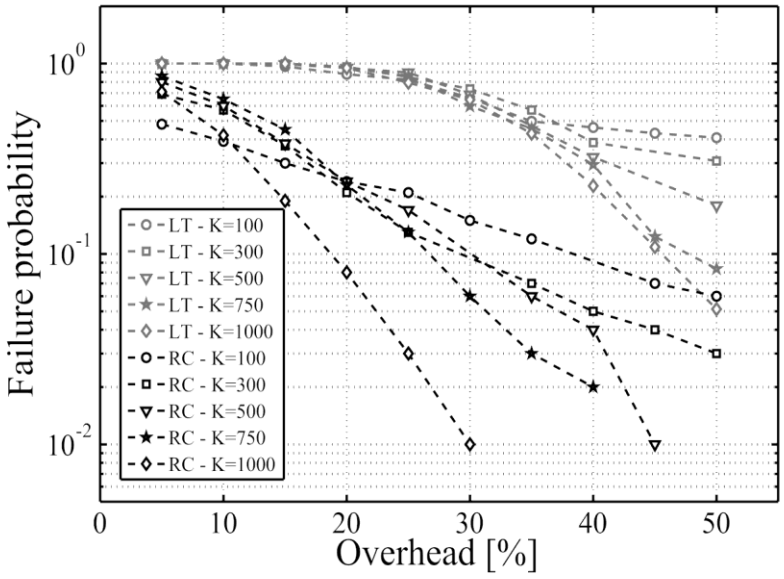

Figure 4.8 – Comparison between LT codes and RCs for the same source packets number and overhead [10].

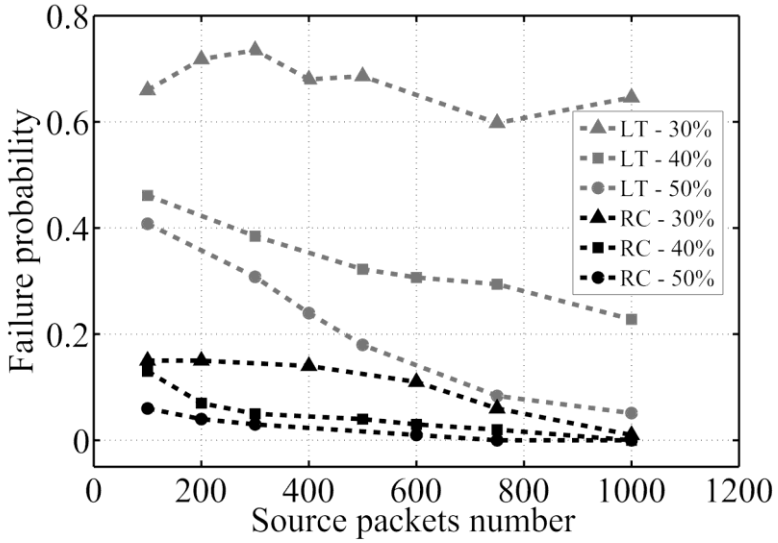

Figure 4.9 – Comparison between LT codes and RCs at constant overhead for the same source packets number [10].

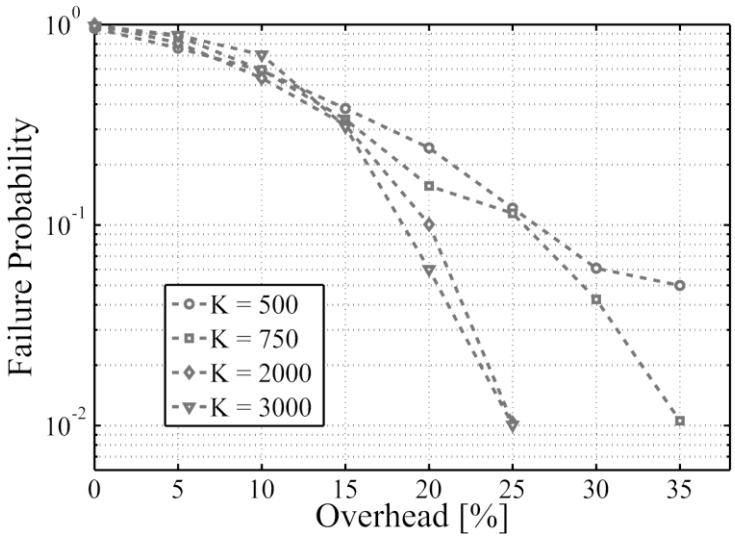

Figure 4.10 – RQ codes at four *K* source packets and several overhead values [10].

4.4.3 GEO Satellite to ground FSO link

In this work, in order to test the rateless codes mentioned in the previous section, I have considered a GEO satellite-to-ground FSO downlink operating at 1 Gbps (OOK modulation and 1518 bytes frame size), taking into account several values of the zenith angle. Moreover, I supposed that additional losses (due to scattering and absorption) are present in the simulated FSO GEO downlink. For this reason, I have assumed that the receiver was not able to detect the useful signal at fading below a -6dB threshold level. The other configuration parameters are shown in Table 4.1 (already introduced in Chapter 2).

Figure 4.11 shows the results of LT codes performance analysis considering: a zenith angle of 80° (corresponding to a strong optical turbulence), several *K* and overhead values. An overhead of 15% is needed to avoid a failure probability of 100%. In fact, LT codes are non-systematic and they also need a minimum received overhead to perform the decoding process. We also note in Figure 4.11 that, with increasing source symbol numbers and at high values of overhead, the recovery probability improves.

Subsequently, I have tested the Raptor and the RaptorQ codes. In Figure 4.12 and Figure 4.13 the test results of, respectively, Raptor and RaptorQ codes are depicted, at 80° zenith angle. In both diagrams, with increasing *K*, the slopes of linear regression (l.r.) augment. Therefore, the higher are the values of overhead and the higher is the number of source packets, the better is the performance of the codes. I have highlighted that, conversely

to LT codes, the failure probability of Raptor and RaptorQ codes decreases already at low overhead values. Moreover, RaptorQ has slightly better recovery capabilities than Raptor, while they show great improvements if compared to LT codes. In fact, considering K=1000 and overhead 30%, the failure probability decreases from 50% (in LT) to 35% (in Raptor) and to 25% (in RaptorQ). Hence, RaptorQ codes should be preferred when optical turbulence conditions are worse.

TABLE 4.1
RYTOV VARIANCE COMPUTATION PARAMETERS

Symbol	Quantity	Value
λ	Wavelength	1.06 μm
w	Wind speed	21 m/s
H	Satellite altitude	35800 km
h_0	Ground station altitude	0 m
A	C_n^2 at ground level	1.7×10^{-14} $m^{-2/3}$

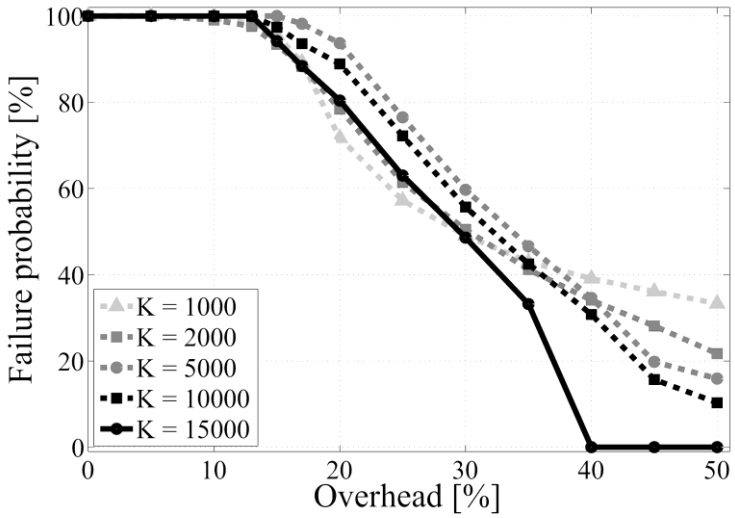

Figure 4.11 – Performance of LT codes at 80° zenith angle, different values of K and several overhead [13].

In conclusion, these simulations showed that, for a zenith angle of 80°, LT codes had good recovery capabilities only considering high values of K (source symbols) and of the overhead. In general, Raptor and especially RaptorQ codes are, instead, able to drastically

mitigate erasure errors already for lower values of *K* and overhead (such as *K*=1000, overhead 20%). I have highlighted that RQ codes provide the best recovering performance, if compared to the other rateless codes, in particular when a high number of *K* packets is required [13].

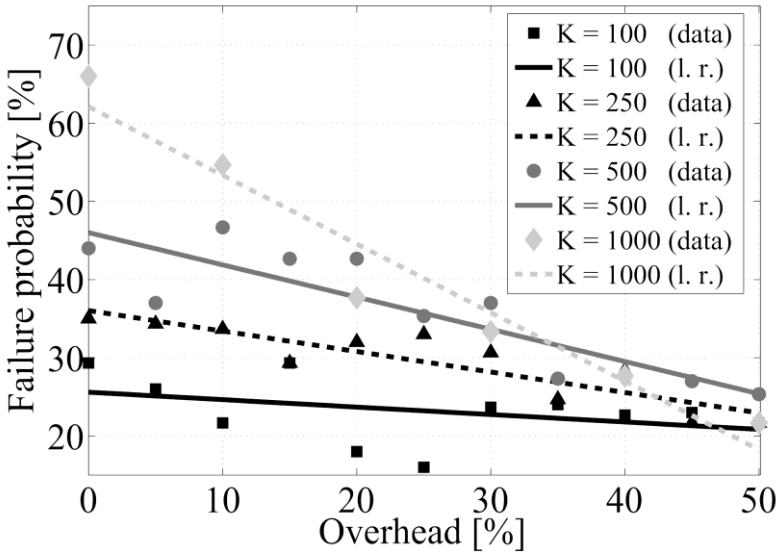

Figure 4.12 – Performance of Raptor codes at 80° zenith angle, different values of *K* and several overhead values [13].

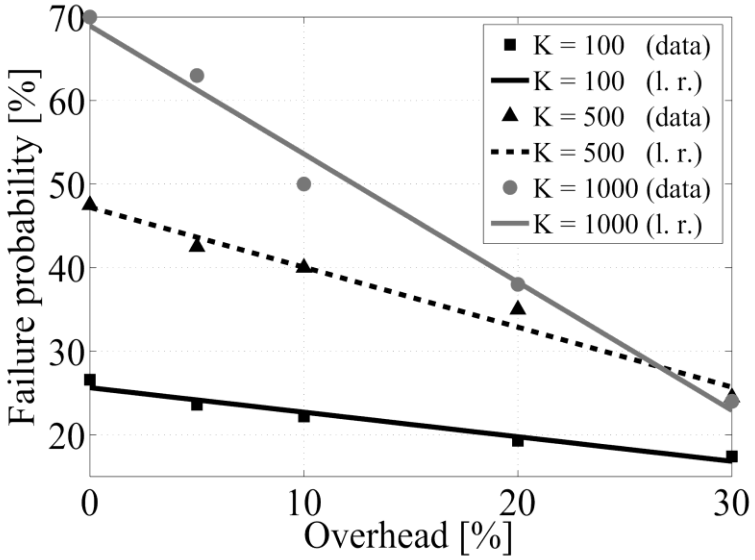

Figure 4.13 – Performance of RaptorQ codes at 80° zenith angle, different values of *K* and several overhead values [13].

References

[1] D.J.C. MacKay, “Fountain codes,” in IEE Proceedings - Communications, vol. 152, no. 6, pp. 1062-1068, 2005.

[2] M. Luby, “LT Codes,” in Proceedings of the 43rd Annual IEEE Symposium on Foundations of Computer Science (FOCS '02), pp. 271–282, 2002.

[3] D.J.C. MacKay, “Information theory, inference, and learning algorithms,” Cambridge University Press, 2003 - (Available from www.inference.phy.cam.ac.uk/mackay/itila/).

[4] A. Shokrollahi, “Raptor Codes,” IEEE Transactions on Information Theory, vol. 52, no. 6, pp. 2551-2567, 2006.

[5] M. Luby, A. Shokrollahi, M. Watson, and T. Stockhammer, “Raptor Forward Error Correction Scheme for Object Delivery,” RFC 5053 - Proposed Standard, IETF, 2007.

[6] J. Lacan, V. Roca, J. Peltotalo, and S. Peltotalo, “Reed-Solomon Forward Error Correction (FEC) Schemes,” RFC 5510 - Standard Tracks, IETF, 2009.

[7] A. Shokrollahi and M. Luby, “Raptor Codes,” Foundations and Trends in Communications and Information Theory, vol. 6, no. 3-4, pp. 213-322, 2011.

[8] M. Luby, A. Shokrollahi, M. Watson, T. Stockhammer, and L. Minder, “RaptorQ Forward Error Correction Scheme for Object Delivery,” RFC 6330 - Proposed Standard, IETF, 2007.

[9] C. Bouras, N. Kanakis, V. Kokinos, and A. Papazois, ““Enhancing reliable mobile multicasting with RaptorQ FEC,” in Proceedings of the 2012 IEEE Symposium on Computers and Communications (ISCC 2012), pp. 000082 – 000087, 2012.

[10] A. Andò, S. Mangione, L. Curcio, S. Stivala, G. Garbo, R. Pernice, A.C. Busacca, "Recovery Capabilities of Rateless Codes on Simulated Turbulent Terrestrial Free Space Optics Channel Model," International Journal of Antennas and Propagation, Article ID 692915, 2013.

[11] P. A. Chou, M. van der Schaar, "Multimedia over IP and wireless networks," Academic press, 2007.

[12] A. Andò, S. Mangione, L. Curcio, S. Stivala, G. Garbo, A. Busacca, G. M. Tosi Beleffi, F. S. Marzano, "Rateless codes Performance tests on terrestrial FSO time-correlated channel model," in Proceeding IEEE of the International Workshop on Optical Wireless (IWOW), pp 1-3, 2012.

[13] A. Andò, G. Messineo, L. Curcio, S. Mangione, P. Gallo, A. C. Busacca, "Rateless codes performance analysis in correlated channel model for GEO Free Space Optics downlinks," in Proceeding IEEE of the International Conference on Space Optical Systems and applications, 2012.

Conclusions

In this thesis, the optical turbulence effects in a Free Space Optical link have been investigated. In particular, I have implemented a high-resolution FSO channel model, which takes into account the temporal covariance of irradiance. My model is able to generate irradiance time-series, in order to predict irradiance fluctuations at the receiver with high temporal resolution. It allows to set several configurable parameters related to the link specifications, turbulence conditions and time resolution. Simulated data extracted by the model are in good agreement with the results obtained by several measurement campaigns performed with different experimental set-ups. In particular, a very good agreement was achieved between the experimental data collected during the measurement campaigns performed and the simulated irradiance time-series. Unfortunately, only weak turbulence conditions were investigated in the experimental measurements that I have performed. This allowed me to verify the effectiveness of the irradiance generators only in the above mentioned conditions. However, the experimental data highlights that, even in the case of weak turbulence, the performance of a FSO link can strongly decrease. At the maximum obtained scintillation index 0.073 (in the chamber set-up) I have obtained very low performance (BER=7.34×10^{-2} and Q-factor=1.45). The results that I have collected from simulations on the performance recovery capabilities of the rateless codes demonstrate that RaptorQ codes offer can be successfully used to improve link performance. In particular, in the case of a 500 m terrestrial FSO link, with a rate of 100 Mbps and a Rytov variance of 1.0, LT codes, with a number of source symbols equal to 1000, are not able to cancel erasure errors, even with a 50% overhead. On the other hand, Raptor codes can remove all the erasure errors, with a 50% overhead, even starting from K = 500. Nonetheless, RaptorQ codes provided the best recovering performance. They work slightly better than Raptor codes and are the best choice, especially when high values of K are required. In addition, in the case of GEO satellite-to-ground FSO downlinks, RaptorQ codes presented the best performance. Simulations showed that, for a zenith angle of 80°, LT codes had good recovery capabilities only considering very high values of source symbols and overhead. As regards Raptor and RaptorQ codes, they were not able to recover all the data at low values of source symbols and overhead. During my work, I have also demonstrated that it is possible to predict that, starting

from an overhead over 35% and K=1000, RaptorQ codes are able to recover all the source data, even in the case of zenith angle of 80°. If compared to the other rateless codes, RaptorQ codes provide, in all conditions, the best recovering performance, especially when a high number of K packets is required. In conclusion, the analysis that I have performed shows that, with a proper setting of the configuration parameters, the rateless codes could be a suitable software solution for fading mitigation in FSO links. Future activities should focus on the experimental test of the rateless codes in several FSO scenarios and, moreover, on the validation of the time-series generator at moderate-to-strong turbulence conditions.